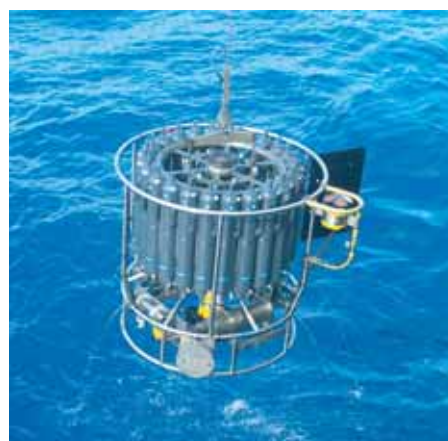# Conservative Space and Time Regularizations for the ICON Model

Marco Giorgetta, Tobias Hundertmark,
Peter Korn, Sebastian Reich, Marco Restelli

Hinweis

Die Berichte zur Erdsystemforschung werden vom Max-Planck-Institut für Meteorologie in Hamburg in unregelmäßiger Abfolge herausgegeben.

Sie enthalten wissenschaftliche und technische Beiträge, inklusive Dissertationen.

Die Beiträge geben nicht notwendigerweise die Auffassung des Instituts wieder.

Die "Berichte zur Erdsystemforschung" führen die vorherigen Reihen "Reports" und "Examensarbeiten" weiter.

Notice

The Reports on Earth System Science are published by the Max Planck Institute for Meteorology in Hamburg. They appear in irregular intervals.

They contain scientific and technical contributions, including Ph. D. theses.

The Reports do not necessarily reflect the opinion of the Institute.

The "Reports on Earth System Science" continue the former "Reports" and "Examensarbeiten" of the Max Planck Institute.

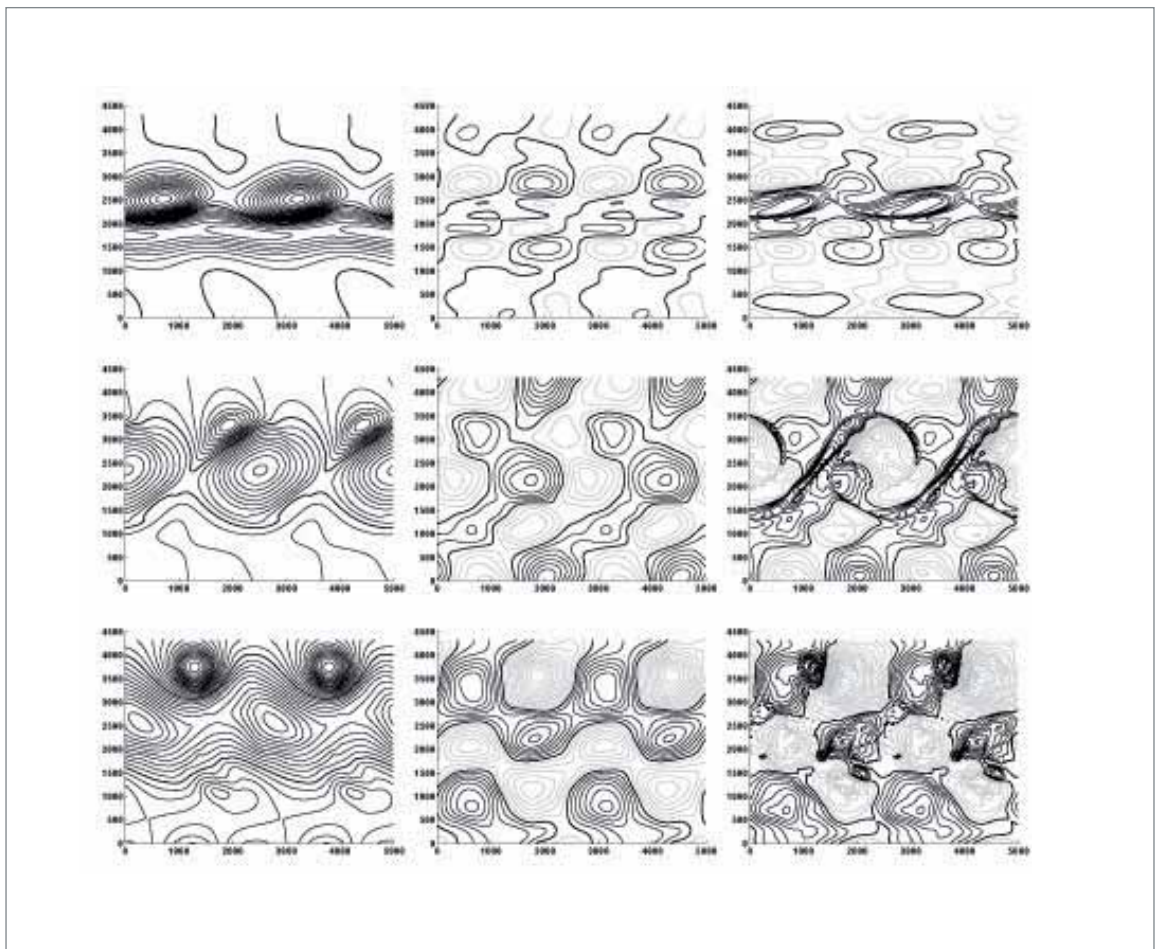# Conservative Space and Time Regularizations for the ICON Model

Marco Giorgetta, Tobias Hundertmark,
Peter Korn, Sebastian Reich, Marco Restelli

Hamburg 2009

Marco Giorgetta [1]
Tobias Hundertmark [2]
Peter Korn [3]
Sebastian Reich [4]
Marco Restelli [5]

1   Atmosphäre im Erdsystem,
    Max–Planck–Institut für Meteorologie, Bundesstraße 53, 20146 Hamburg, Germany
    (marco.giorgetta@zmaw.de)

2   Institut für Mathematik,
    Universität Potsdam, Am Neuen Palais 10, D-14469 Potsdam, Germany
    (hundertm@uni-potsdam.de)

3   Ozean im Erdsystem,
    Max–Planck–Institut für Meteorologie, Bundesstraße 53, 20146 Hamburg, Germany
    (peter.korn@zmaw.de)

4   Institut für Mathematik,
    Universität Potsdam, Am Neuen Palais 10, D-14469 Potsdam, Germany
    (sreich@math.uni-potsdam.de)

5   Ozean im Erdsystem,
    Max–Planck–Institut für Meteorologie, Bundesstraße 53, 20146 Hamburg, Germany
    (marco.restelli@zmaw.de)

Conservative Space and
Time Regularizations
for the ICON Model

Marco Giorgetta, Tobias Hundertmark,
Peter Korn, Sebastian Reich, Marco Restelli

Hamburg 2009

CONSERVATIVE SPACE AND TIME REGULARIZATIONS FOR THE ICON MODEL

MARCO GIORGETTA*, TOBIAS HUNDERTMARK[†], PETER KORN[‡], SEBASTIAN REICH[§], AND MARCO RESTELLI[¶]

Abstract. In this article, we consider two modified (regularized) versions of the shallow water equations which are of potential interest for the construction of global oceanic and atmospheric models. The first modified system is the Lagrangian averaged α shallow water system, which involves the use of a regularized advection velocity and which has been recently proposed as a turbulence parametrization for ocean models in order to avoid an excessive damping of the computed solution. The second modified system is the pressure regularized τ shallow water system, which provides an alternative to traditional semi-implicit time integration schemes and which results in larger freedom in the design of the time integrator and in a better treatment of nearly geostrophic flows. The two modified systems are both nondissipative, in that they do not result in an increase of the overall dissipation of the flow. We first show how the numerical discretization of the two regularized equation sets can be constructed in a natural way within the finite difference formulation adopted for the ICON general circulation model currently under developed at the Max Planck Institute for Meteorology and at the German Weather Service. The resulting scheme is then validated on a set of idealized tests in both planar and spherical geometry, and the effects of the considered regularizations on the computed solution are analyzed concerning: stability properties and maximum allowable time steps, similarities and differences in the behavior of the solutions, discrete conservation of flow invariants such as total energy and enstrophy. Our analysis should be considered as a first step toward the use of the regularization ideas in the simulation of more complex and more realistic flows.

AMS subject classifications. 65M06, 65M20, 35L65, 86A05, 86A10

Key words. shallow water equations, nondissipative regularizations, Lagrangian averaged equations, two-dimensional turbulence, pressure regularizations, semi-implicit methods

1. Introduction. Numerical modeling of atmospheric and oceanic flows is a multiscale problem for which the following two complementary aspects can be identified:
  1. treatment of turbulence (subgridscale modeling) and
  2. treatment of scale-separated phenomena.
Under the first aspect, one intends to include effects of unresolved scales by using heuristically motivated turbulence models. Under the second aspect, one tries to eliminate "undesirable" time and length scales by making approximations to the complete model equations based on the idealization of an asymptotic scale separation. The derivation of turbulence models generally faces the problem of closure under averaging. The treatment of scale-separated phenomena via approximated models is unsatisfactory, since the approximated models are valid only under certain flow regimes and one is faced with a whole hierarchy of filtered models with limited area of applicability. Moreover, a fundamental difficulty that is shared by both approaches mentioned above is to reproduce, possibly in a modified form, the conservation and balance relations which characterize the original model, such as, for suitable conditions, linear and angular momentum conservation and energy balance, within the approximated one. Such properties, together with their discrete counterparts in the numerical discretization, are highly relevant especially when considering the evolution of atmospheric and oceanic flows over very long times (i.e. from tens to thousands of years), as it is typically done in climate simulations, because they reduce the spurious trends in the simulation.

Our approach consists in studying both phenomena of subgrid turbulence and scale separation in a unified way by means of *nondissipative regularizations* of the underlying model equations. By regularization we mean a family of models $M(\epsilon)$ depending on a continuous parameter $\epsilon > 0$, such that for $\epsilon \to 0$ the regularizations $M(\epsilon)$ approach the full model, denoted by $M(0)$, in a sense that has to be

---

*Atmosphäre im Erdsystem, Max–Planck–Institut für Meteorologie, Bundesstraße 53, 20146 Hamburg, Germany (`marco.giorgetta@zmaw.de`).

[†]Institut für Mathematik, Universität Potsdam, Am Neuen Palais 10, D-14469 Potsdam, Germany (`hundertm@uni-potsdam.de`).

[‡]Ozean im Erdsystem, Max–Planck–Institut für Meteorologie, Bundesstraße 53, 20146 Hamburg, Germany (`peter.korn@zmaw.de`).

[§]Institut für Mathematik, Universität Potsdam, Am Neuen Palais 10, D-14469 Potsdam, Germany (`sreich@math.uni-potsdam.de`).

[¶]Ozean im Erdsystem, Max–Planck–Institut für Meteorologie, Bundesstraße 53, 20146 Hamburg, Germany (`marco.restelli@zmaw.de`).

determined; a regularization is then nondissipative if, besides ensuring mass conservation, it does not result in additional dissipation terms in the overall momentum and energy balances. In particular, we consider the following two regularization approaches:

1. *α-Models via Velocity Regularization.* The α model regularizes the advection velocity and includes an additional term into the equations to retain a set of (modified) conservation properties. The regularization is performed with respect to the spatial scale, i.e., $\epsilon = \alpha$ and α is the smallest scale that is resolved explicitly. In numerical implementations, α is proportional to the grid-size Δx.

2. *τ-Models via Pressure Regularization.* The τ model smoothes the pressure gradient. The regularization is performed with respect to a given time-scale τ and the parameter $\epsilon = \tau$ is hence a function of the desired time step Δt.

The underlying hypothesis is that the α- and τ-regularizations provide a modification of the original equations that is more accessible to numerical modeling and at the same time retains important features of the original model equations. The goal of this article is to demonstrate some evidence for this assertion. We investigate the effect of the α- and the τ- regularization in the context of the ICON shallow-water [4, 3] model and consider in particular the interaction between the two regularizations and the discrete model numerics.

2. Theory of α- and τ-Models. Both the velocity and the pressure regularizations have been originally obtained starting from a decomposition into mean and fluctuating parts of the Lagrangian trajectories of the flow, within the framework of the generalized Lagrangian mean (GLM) theory of Andrews and McIntyre [1]. In the GLM approach, the current position of a Lagrangian fluid trajectory is written as $\mathbf{x}^{\xi}(t) \equiv \mathbf{x}(t) + \boldsymbol{\xi}(\mathbf{x}(t), t)$, where $\mathbf{x}(t)$ is the mean position, defined for a suitable averaging operator, for instance an ensemble average, and $\boldsymbol{\xi}(\mathbf{x}, t)$ denotes the fluctuating displacement about the mean. For incompressible flows, inserting the trajectory decomposition into the variational principle from which the dynamical equations are derived, together with specific assumptions on the statistics of the fluctuations, results in the Lagrangian Averaged α Equations, characterized by the presence of a regularized velocity field [19]. For compressible flows, the trajectory decomposition can be used in the Lagrangian form of the continuity equation to obtain pressure regularized fluid equations [8]. The pressure regularized equations in [8] constitute a particular class of τ models and we notice more generally that alternative derivations of both regularized systems are also possible. On the one hand, in fact, the α model, can be derived through the so-called Kelvin filtering, for which we refer to [10] and to [17], exercise 4 page 85, as well as from continuum mechanics considerations, as done in [11, 6], or by direct manipulation of the flow equations, as in [28, 16]. Such a model has also been analyzed from a Large Eddy Simulation (LES) perspective in [12, 13, 14], together with a closely related model know as the Leray model, since the original work [24]. The τ model, on the other hand, can also be derived from an analysis of the regularizing effect inherent in numerical semi-implicit time integration techniques, as shown in [33, 38, 34]. Although both regularizations can be applied to a whole hierarchy of models that are used in geophysical fluid dynamics (see for instance [20] and [23]), for simplicity we will focus in this paper on the shallow water system

$$\begin{array}{rcl} \partial_t \mu + \nabla \cdot (\mu \mathbf{v}) & = & 0 \\ \partial_t \mathbf{v} + \mathbf{v} \cdot \nabla \mathbf{v} + f \mathbf{v}^{\perp} + g \nabla \mu & = & \nu \nabla \cdot (\mu \nabla \mathbf{v}) \end{array} \tag{2.1}$$

on an f-plane, where $\mathbf{v}$ is the horizontal velocity field, μ is the layer-depth, g is the gravitational constant, f is the Coriolis parameter, $\mathbf{v}^{\perp} = \mathbf{k} \times \mathbf{v}$, $\mathbf{k}$ being a vertical unit vector, and ν is the molecular viscosity of the fluid.

System (2.1) is denoted in the following as SW-0, in order to emphasize that it can be recovered from the velocity and pressure regularized systems, denoted by SW-α and SW-τ, respectively, when the regularization parameter is set to zero. The aim of regularization is to derive modified versions of (2.1) the solution of which can be well represented computationally for given spatial and/or temporal resolution. In order to distinguish these solutions from those of the original problem (2.1), we will use the notation $\mathbf{u}$ and h for the velocity and the layer depth of the regularized systems, respectively. From the analytical viewpoint [19, 8], $\mathbf{u}$ and h can be expected to belong to a functional space with higher regularity than the original solution $\mathbf{v}$, μ. We emphasize here that the two solutions of SW-α and SW-τ

are different from each other; nevertheless, for simplicity, we employ for both the same notation, since the distinction is usually clear from the context. A subscript is introduced whenever the context might be ambiguous. For the same reason, we avoid differentiating the notation for the diagnostic quantities: vorticity and dynamic pressure. In the following two subsections we will introduce the SW-α and SW-τ models in more detail. Relations and analogies between both classes of regularizations, and in particular between $\mathbf{v}$ and $\mathbf{u}$ velocities and between μ and h free surface elevations, will be discussed in § 2.3.

2.1. Some Background on the SW-α Model. Preferred turbulence closure schemes in general circulation models (GCM) are linear diffusion schemes; examples of this are the ECHAM5 GCM [35] of the Max Planck Institute for Meteorology or the GME, the current operational GCM of the German Weather Service [26]. In contrast to this approach, the outcome of the GLM formalism in the Lagrangian averaged turbulence model [20, 41], also known as viscous Camassa–Holm equations, is a modification of the nonlinear advection term in the momentum equation by smoothing the advection velocity of the fluid. The resulting formulation has the following attractive features: no additional dissipation is introduced and basic characteristics of the flow, such as the conservation of circulation, are preserved. The regularized problem is mathematically well posed, and the expected behavior of the energy spectrum is well captured in three dimensional computations. In terms of the governing equations, in the SW-α model we substitute (2.1) with

$$
\begin{aligned}
\partial_t \tilde{h} + \nabla \cdot \left(\tilde{h} \tilde{\mathbf{u}} \right) &= 0 \\
\partial_t \mathbf{u} + \tilde{\mathbf{u}} \cdot \nabla \mathbf{u} + \sum_{j=1}^{2} u_j \nabla \tilde{u}_j + f \tilde{\mathbf{u}}^\perp + \nabla \left(g \tilde{h} + p_D - \mathbf{u} \cdot \tilde{\mathbf{u}} \right) &= \nu \nabla \cdot \left(\tilde{h} \nabla \mathbf{u} \right),
\end{aligned}
\tag{2.2}
$$

where $p_D = \mathbf{u} \cdot \tilde{\mathbf{u}} - \frac{1}{2} \left(|\tilde{\mathbf{u}}|^2 + \alpha^2 |\nabla \tilde{\mathbf{u}}|^2 \right)$ is a dynamic pressure and the velocity $\tilde{\mathbf{u}}$ is defined via the relation

$$
\mathcal{H}_\alpha \tilde{\mathbf{u}} = \mathbf{u}, \qquad \mathcal{H}_\alpha = 1 - \frac{\alpha^2}{\tilde{h}} \nabla \cdot \left(\tilde{h} \nabla \right).
\tag{2.3}
$$

The spatial length scale α in the Helmholtz operator $\mathcal{H}_\alpha$ is typically of the order of the mesh-size and, hence, we are interested in solutions of (2.2) for which $\tilde{\mathbf{u}}$ is close to $\mathbf{u}$ on the computationally resolved scales. The regularized free surface elevation $\tilde{h}$ is defined by $\mathcal{H}_\alpha \tilde{h} = h$. The reason for introducing both h and $\tilde{h}$, although only $\tilde{h}$ appears in (2.2), is twofold: on the one hand, a geostrophically balanced initial condition can be obtained by using $\mathbf{u} \approx \mathbf{v}$ and $h \approx \mu$ to initialize $\tilde{\mathbf{u}}$ and $\tilde{h}$, respectively, i.e.,

$$
f \tilde{\mathbf{u}}^\perp + g \nabla \tilde{h} = 0 \iff f \mathbf{u}^\perp + g \nabla h = 0.
\tag{2.4}
$$

On the other hand, h and $\tilde{h}$ will turn out to be directly comparable to the homologous quantities in SW-τ.

The derivation of the SW-α system (2.2) and (2.3) relies on the hypothesis that the covariant matrix of the fluctuating component $\boldsymbol{\xi}$ of the displacement appearing in the GLM formalism is an isotropic tensor which is constant in space and time, so that it is possible to introduce $\alpha \in \mathbb{R}^+ \cup \{0\}$ such that

$$
\langle \boldsymbol{\xi} \otimes \boldsymbol{\xi} \rangle = \alpha^2 \mathcal{I},
$$

where $\langle \cdot \rangle$ denotes spatial averaging at a fixed time and $\mathcal{I}$ is the identity tensor [20, 19]. Since in the present work we consider periodic domains without boundaries, the assumption of isotropy and homogeneity is justified; in more realistic situations however, the presence of boundaries might require the use of a complete anisotropic model, including a nontrivial evolution equation for $\langle \boldsymbol{\xi} \otimes \boldsymbol{\xi} \rangle$ [19]. In the present study, we are particularly concerned with two properties of the SW-α system: the fact that it reproduces, for the inviscid case and for suitable boundary conditions, the conservations of energy and potential enstrophy which characterize the SW-0 case (i.e., it is a nondissipative regularization) and the fact that, thanks to the modification of the advection term, spatial scales smaller than α do not take part into the nonlinear interaction and are passively advected by the flow. The conservation of energy and potential enstrophy takes the form

$$
E_\alpha = \frac{1}{2} \int_\Omega \tilde{h} \left(|\tilde{\mathbf{u}}|^2 + \alpha^2 |\nabla \tilde{\mathbf{u}}|^2 + g \tilde{h} \right) d\mathbf{x} = const
\tag{2.5}
$$

and

$$S = \frac{1}{2} \int_\Omega \tilde{h} q^2 \, d\mathbf{x} = const, \tag{2.6}$$

where Ω is the domain occupied by the flow and the potential vorticity is $q = \tilde{h}^{-1}\eta$, with $\eta = \mathbf{k} \cdot \nabla \times \mathbf{u} + f$. The fact that the small scales do not take part in the nonlinear interactions then affects the spectral distribution of E_α and S. A further consequence of the Lagrangian averaging, and in particular of the use of the smooth velocity $\tilde{\mathbf{u}}$ in the continuity equation $(2.2)_1$, is a slowdown of the gravity waves (notice that a subscript is used to denote single equations within a referenced formula). This effect is analogous to what is discussed in § 2.2 for SW-τ, to such an extent that the two regularizations coincide in the linearized, non-rotating case. The SW-α model has been investigated in some detail for the case of two and three dimensional incompressible turbulence in [5, 27, 29, 25], and one of the key findings in this respect is that the energy spectrum of the modified energy E_α in (2.5) exhibits a sharper roll-off than the energy of the unfiltered Navier–Stokes equations. The potential of such a model for geophysical applications has then been considered in [41, 22, 18, 31].

2.2. Some Background on τ-Regularized Models. As already mentioned, alternative derivations exist for the pressure regularized model. In this section, we briefly sketch the derivation of SW-τ from an analysis of a classical semi-implicit time stepping technique for the numerical integration of the unfiltered problem (2.1), following [33, 38, 34].

The main justification for the use of semi-implicit time integrators for geophysical fluid dynamics applications, and in particular for the shallow water system (2.1), is the assumption that the flow is composed of slow, large scale modes and of fast, small scale modes, with only the former ones being of meteorological interest. As a consequence, an accurate representation of the fast modes is not required, and a large dispersion error for such modes is an acceptable price in order to obtain an efficient numerical scheme. In order now to derive the SW-τ model, the semi-implicit time-stepping method is first interpreted as a form of "regularization" of the layer-depth μ, depending on the temporal scale $\tau = \Delta t/2$, and this regularization effect is then transferred directly into the continuous equations by an appropriate modification of the velocity equation $(2.1)_2$. The main advantage of this procedure is that the modified system can then be discretized explicitly in time using a time step analogous to the one permitted by a semi-implicit scheme. More precisely, a careful analysis of the semi-implicit method and of the associated elliptic problem suggests the introduction of the SW-τ system

$$\begin{aligned}
\partial_t h + \nabla \cdot (h\mathbf{u}) &= 0 \\
\partial_t \mathbf{u} + \mathbf{u} \cdot \nabla \mathbf{u} + f\mathbf{u}^\perp + g\nabla\tilde{h} &= \nu\nabla \cdot \left(\tilde{h}\nabla\mathbf{u}\right),
\end{aligned} \tag{2.7}$$

where $\tilde{h}$ is the regularized layer depth obtained from

$$\mathcal{H}_\tau \tilde{h} = h + \Pi, \quad \mathcal{H}_\tau = 1 - \tau^2 g H_0 \nabla \cdot \nabla \tag{2.8}$$

where $\tau \geq 0$ is a parameter with the dimension of time and H_0 is a mean reference value for the layer depth. As for the SW-α model, we assume that $\tilde{h}$ is close to h on the computationally resolved scales. Concerning the definition of Π in (2.8), letting $\zeta = \mathbf{k} \cdot \nabla \times \mathbf{u}$ and denoting by $J(\cdot, \cdot)$ the Jacobian operator, we distinguish the following cases:

- τ-regularization without balance

$$\Pi = 0; \tag{2.9}$$

- τ-regularization with linear balance

$$\Pi = -\tau^2 H_0 f \zeta; \tag{2.10}$$

- τ-regularization with non-linear balance

$$\begin{aligned}
\Pi &= \tau^2 H_0 \nabla \cdot \left[\mathbf{u} \cdot \nabla \mathbf{u} + f\mathbf{u}^\perp\right] \\
&= -\tau^2 H_0 f \zeta - 2\tau^2 H_0 J(u_1, u_2) + \tau^2 H_0 \left(\mathbf{u} \cdot \nabla + \nabla \cdot \mathbf{u}\right) \nabla \cdot \mathbf{u}.
\end{aligned} \tag{2.11}$$

Notice that, if Π is defined as in (2.11), no regularization of the layer depth takes place, i.e. $h = \tilde{h}$, under the nonlinear balance

$$g\nabla \cdot \nabla h - f\zeta - 2J(u_1, u_2) = 0, \qquad \nabla \cdot \mathbf{u} = 0,$$

which reduces to linear geostrophic balance when the Jacobian operator vanishes. However, unlike in reduced geostrophic models, the nonlinear balance is not strictly enforced; equation (2.11) treats balance in a scale dependent manner, depending on the choice of the time scale τ and $\sqrt{gH_0}$, the phase velocity of gravity waves in a layer of depth H_0. Notice also that both SW-α and SW-τ involve the solution of a modified Helmholtz problem, for the computation of the regularized velocity in the first case and for the computation of the regularized layer depth in the second case. A length scale $\beta = \tau\sqrt{gH_0}$ can be defined for the SW-τ model for comparison to the length scale α of the SW-α model. Concerning the nondissipative nature of the pressure regularization, it can be verified that (2.7) results, in the inviscid case, in the potential enstrophy conservation (2.6). Finally, a characterization of the effect of SW-τ on the gravity wave propagation is provided in § 3.3.2.

2.3. Analogies and relations among SW-0, SW-α, SW-τ and LES turbulence models. Since the solutions of SW-α and SW-τ are different from each other as well as from the solution of SW-0, and since both SW-α and SW-τ introduce additional variables $\tilde{\mathbf{u}}$ and $\tilde{h}$, the question arises of how to establish a correspondence among the variables of the regularized systems and those of the original problem SW-0. We address this topic borrowing some ideas from the LES approach [2].

To start with, let us consider the shallow water problems (2.1), (2.2) and (2.7) in their continuous formulation, let us assume that SW-0 is the "true" mathematical model of the physical flow, and let us denote by $\mathbf{v}$ and μ a solution of (2.1) (such a solution can be viewed also as the result of a direct numerical simulation of the flow). Concerning the pressure regularization, we assume that $\mathbf{u}_\tau$ and h_τ of (2.7) are approximations of $\mathbf{v}$ and μ, respectively, and that $\tilde{h}_\tau$ is a filtered free surface elevation introduced to modify the propagation of the fast (unresolved) gravity waves on time-scales smaller than τ. Concerning the velocity regularization, we proceed as follows. We first consider the regularized system obtained by simply filtering the advection velocity in $(2.1)_2$

$$
\begin{aligned}
\partial_t h_L + \nabla \cdot (h_L \mathbf{u}_L) &= 0 \\
\partial_t \mathbf{u}_L + \tilde{\mathbf{u}}_L \cdot \nabla \mathbf{u}_L + f\mathbf{u}_L^\perp + g\nabla h_L &= \nu\nabla \cdot (h_L \nabla \mathbf{u}_L),
\end{aligned}
\qquad (2.12)
$$

where $\tilde{\mathbf{u}}_L$ is obtained from $\mathbf{u}_L$ using the filter (2.3). System (2.12) corresponds to the Leray model discussed in [12, 13, 14] and, extending the viewpoint given in these references for incompressible LES to the compressible, low Mach number case considered here, we can regard the velocity $\tilde{\mathbf{u}}_L$ as a filtered version of $\mathbf{v}$ and $\mathbf{u}_L$ as an approximate deconvolution of $\tilde{\mathbf{u}}_L$ [2] (since the resolution of $\mathbf{u}_L$ is determined by the spatial grid resolution); $\mathbf{u}_L$ should thus approximate the grid interpolated velocity $\mathbf{v}$, and the same relation is assumed to hold between h_L and μ. The construction of SW-α from (2.12) requires now two modifications. The first modification is the introduction of the additional terms quadratic in $\mathbf{u}_\alpha$ and $\tilde{\mathbf{u}}_\alpha$ appearing in $(2.2)_2$; this exactly corresponds to what is done in the incompressible case, where it is motivated by the need of restoring the Kelvin circulation theorem. The second modification is the substitution of h with $\tilde{h}$, and hence the use of the filtered continuity equation

$$\partial_t \tilde{h}_\alpha + \nabla \cdot (\tilde{h}_\alpha \tilde{\mathbf{u}}_\alpha) = 0, \qquad (2.13)$$

where the approximation $\widetilde{h_\alpha \mathbf{u}_\alpha} \approx \tilde{h}_\alpha \tilde{\mathbf{u}}_\alpha$ has been made. This modification has no counterpart in the incompressible case and is motivated by the restoration of energy and enstrophy conservation in the compressible system. This second modification also has the side effect of modifying the gravity wave propagation in SW-α, as already mentioned in § 2.1. As shown in [41], in the non-rotating case this is equivalent to the effect of semi-implicit time-stepping on a linearized equation level and, hence, is linearly equivalent to the SW-τ regularization for $\beta = \alpha$.

So far, we have identified some parallelisms among the SW-α and SW-τ models as they have been independently proposed in previous works. The aforementioned considerations, however, can also provide the starting point for introducing a new regularized model, resulting from the combination of the SW-α

momentum equation with the SW-τ regularization, namely

$$\partial_t h + \nabla \cdot (h\mathbf{u}) = 0$$

$$\partial_t \mathbf{u} + \tilde{\mathbf{u}} \cdot \nabla \mathbf{u} + \sum_{j=1}^{2} (u_j - \tilde{u}_j) \nabla u_j + f\mathbf{u}^\perp + g\nabla\tilde{h} = \nu\nabla \cdot \left(\tilde{h}\nabla\mathbf{u}\right). \tag{2.14}$$

together with

$$\mathcal{H}_\alpha \tilde{\mathbf{u}} = \mathbf{u}, \qquad \mathcal{H}_\tau \tilde{h} = h + \Pi. \tag{2.15}$$

In (2.14), the nonlinear advection is treated as in SW-α, thereby resulting in modified energy and enstrophy cascades, while the pressure gradient term is treated as in SW-τ, thereby ensuring that large time steps can be taken in the numerical integration. A potential advantage of this approach is the independent choice of the two regularization parameters τ and α. Another important aspect of (2.14) is that it recovers the two-dimensional Navier–Stokes-α system in the incompressible case (as does SW-α) and it recovers SW-τ whenever the nonlinearity is negligible. As a consequence, linear Rossby waves are not retarded by (2.14) as they are in SW-α, provided either (2.10) or (2.11) is used. Note that the nonlinear balance relation (2.11) should be modified to

$$\Pi = \tau^2 H_0 \nabla \cdot \left[\tilde{\mathbf{u}} \cdot \nabla \mathbf{u} + \sum_{j=1}^{2} (u_j - \tilde{u}_j) \nabla \tilde{u}_j + f\mathbf{u}^\perp\right] \tag{2.16}$$

while the linear balance formulation (2.10) remains unchanged. Finally, we mention that the regularization of the velocity field could be simplified to

$$\left(1 - \alpha^2 \nabla \cdot \nabla\right) \tilde{\mathbf{u}} = \mathbf{u}. \tag{2.17}$$

3. Numerical Approximation of the Regularized Models. We consider in this section the numerical approximation of the regularized models SW-α and SW-τ, introduced in § 2.1 and § 2.2, respectively. To this end, two elements are worth noting. The first one is that transferring the regularization effects to the continuous model results in a significant freedom in the design of the numerical discretization. The second one is that such a discretization should, in principle, preserve the main features of the regularized models, and in particular the conservation laws (2.5) and (2.6). Previous works on this topic have considered finite difference approaches on quadrilateral grids [33, 38, 34, 18, 31], or, for SW-α only, pseudospectral methods [5, 29, 27, 25]. Finite differences on regular quadrilateral grids are known to posses very good dispersion and accuracy properties, but they are not necessarily the optimal solution in spherical geometry, since in this case one has to deal with pole singularities or non-orthogonal grids or non-homogeneous distributions of the grid points (see [32] and the references therein). Spectral methods are widely used in current GCMs on spherical geometry. They have optimal dispersion properties, are useful for the investigation of turbulent flows, and greatly simplify the solution of the elliptic problems (2.3) and (2.8), but due to the cost of global communication, they might not be competitive with grid point methods for very high resolution GCMs on distributed memory computers. For these reasons, a finite difference formulation based on triangular icosahedral grids has been chosen as the basis for the ICON GCM (see [4] and the references therein for further details) and, since our final goal is to include the space and time regularizations in ICON, we consider in this paper this latter formulation. Hence, we need to extend the approach of [4] to SW-α and SW-τ, thus obtaining a numerical scheme which is different from those already described in the literature. After summarizing the method of [4] in § 3.1, we illustrate the extension to the regularized systems in § 3.2. An off-centering procedure of SW-α and SW-τ, which is useful to avoid an unphysical accumulation of energy in short wavelength gravity waves, is proposed in § 3.3. Finally, the discrete conservation properties of the resulting numerical scheme are discussed in § 3.4.

3.1. The ICON Shallow Water Model. We summarize in this section the discretization proposed in [4] for the SW-0 system. In doing this, we also address the treatment of the diffusion term, omitted in [4], since it is strongly related to the numerical treatment of SW-α. The required notation is introduced in § 3.1.1, in § 3.1.2 the approximate reconstruction and differentiation operators are defined and the discrete approximation of the continuous SW-0 problem is then discussed in § 3.1.3 and § 3.1.4.

3.1.1. Notation. Let Ω be the computational domain represented by either a rectangle $[0\,,L_x)\times[0\,,L_y)$ with periodic boundary conditions or by the sphere of radius R_{Earth}, and let $\mathscr{T}_\lambda$ denote a Delaunay triangulation of Ω, i.e. a partition of Ω into $\mathcal{N}_{cell}$ closed non-overlapping triangular cells c such that none of the cell vertices lies inside the circumcircle of any cell. In the following, it is understood that all the geometric quantities are computed with respect to the appropriate metric defined on Ω. The boundary and the area of c are denoted by ∂c and $|c|$, respectively. The set of the $\mathcal{N}_{edge}$ edges l of the triangulation is denoted by $\mathscr{L}_\lambda$, and we denote by $|l|$ the length of l. We let $\lambda = \max_{l\in\mathscr{L}_\lambda}|l|$. A dual grid, or Voronoi tessellation, $\mathscr{D}_\lambda$ is naturally associated to $\mathscr{T}_\lambda$ as the collection of the $\hat{\mathcal{N}}_{cell}$ cells $\hat{c}$ given by the closures of the sets of all points of Ω that are closer to one vertex of $\mathscr{T}_\lambda$ than to any other vertex. The set of the $\hat{\mathcal{N}}_{edge}$ edges $\hat{l}$ of $\mathscr{D}_\lambda$ is denoted by $\hat{\mathscr{L}}_\lambda$, and we denote by $|\hat{l}|$ the length of $\hat{l}$. It can be verified that $\hat{\mathcal{N}}_{edge} = \mathcal{N}_{edge}$. Each edge $l \in \mathscr{L}_\lambda$ intersects exactly one edge $\hat{l} \in \hat{\mathscr{L}}_\lambda$, which will be denoted by $\hat{l}_l$, and the converse is also true. We have $\hat{l}_l \perp l$. To each $l \in \mathscr{L}_\lambda$ a normal unit vector $\mathbf{N}_l$ is associated, with arbitrarily chosen orientation, as well as a tangential unit vector $\mathbf{T}_l$ such that

$$\mathbf{N}_l \times \mathbf{T}_l = \mathbf{k}_l. \tag{3.1}$$

In (3.1), $\mathbf{k}_l$ is a unit vector normal to Ω and directed toward increasing vertical (flat geometry) or radial (spherical geometry) coordinates. A pair of unit vectors is also associated to each $\hat{l} \in \hat{\mathscr{L}}_\lambda$ by $\hat{\mathbf{N}}_{\hat{l}} = \mathbf{T}_{l_{\hat{l}}}$, $\hat{\mathbf{T}}_{\hat{l}} = -\mathbf{N}_{l_{\hat{l}}}$, so that $\hat{\mathbf{N}}_{\hat{l}} \times \hat{\mathbf{T}}_{\hat{l}} = \mathbf{k}_{\hat{l}}$. To each pair $c \in \mathscr{T}_\lambda$, $l \in \partial c$, two normal unit vectors $\mathbf{n}_{c,l}$ and $\mathbf{t}_{c,l}$ are associated such that $\mathbf{n}_{c,l}$ is the outward unit vector on l with respect to c and $\mathbf{n}_{c,l} \times \mathbf{t}_{c,l} = \mathbf{k}_l$. Unit vectors $\hat{\mathbf{n}}_{\hat{c},\hat{l}}$ and $\hat{\mathbf{t}}_{\hat{c},\hat{l}}$ are analogously associated to each pair $\hat{c} \in \mathscr{D}_\lambda$, $\hat{l} \in \partial \hat{c}$. A generic scalar field ϕ is represented by its cell averaged values on either $c \in \mathscr{T}_\lambda$, denoted ϕ_c, or on $\hat{c} \in \mathscr{D}_\lambda$, denoted $\phi_{\hat{c}}$. A generic vector field $\boldsymbol{\chi}$ is represented by its edge averaged normal and tangential components on $l \in \mathscr{L}_\lambda$, denoted by χ_{N_l} and χ_{T_l}, respectively. The normal and tangential components on $\hat{l} \in \hat{\mathscr{L}}_\lambda$ are immediately obtained as

$$\begin{array}{rcl} \chi_{\hat{N}_{\hat{l}}} & = & \chi_{T_{l_{\hat{l}}}} \\ \chi_{\hat{T}_{\hat{l}}} & = & -\chi_{N_{l_{\hat{l}}}}. \end{array}$$

Finally, for $l \in \mathscr{L}_\lambda$ we denote by c_{1_l} and c_{2_l} the two cells such that $l = \partial c_{1_l} \cap \partial c_{2_l}$ and $\mathbf{N}_l$ points from c_{1_l} to c_{2_l} and, symmetrically, for $\hat{l} \in \hat{\mathscr{L}}_\lambda$ we denote by $\hat{c}_{1_{\hat{l}}}$ and $\hat{c}_{2_{\hat{l}}}$ the two cells such that $\hat{l} = \partial \hat{c}_{1_{\hat{l}}} \cap \partial \hat{c}_{2_{\hat{l}}}$ and $\hat{\mathbf{N}}_{\hat{l}}$ points from $\hat{c}_{1_{\hat{l}}}$ to $\hat{c}_{2_{\hat{l}}}$.

3.1.2. Discrete operators. As it will be clear from § 3.1.3, the use of a staggered finite difference approach implies that each variable is directly available only on a limited set of grid elements, typically represented by either the primal cells c or the dual cells $\hat{c}$ or the edges l. Whenever a variable is required on a different set of grid elements, a reconstruction operator is required. The complete set of reconstruction operators used in the numerical approximation of SW-0, SW-α and SW-τ is listed in Tab. 3.1. Notice that, in this section, ϕ and $\boldsymbol{\chi}$ represent two generic scalar and vector fields, respectively. With the exception of $\mathcal{R}_{\hat{c}\to l}$, the definition of which is important for enstrophy conservation and will be

operator	from		to	
$\mathcal{R}_{c\to l}$	primal cells	ϕ_c	edges	ϕ_l
$\mathcal{R}_{c\to\hat{c}}$	primal cells	ϕ_c	dual cells	$\phi_{\hat{c}}$
$\mathcal{R}_{\hat{c}\to l}$	dual cells	$\phi_{\hat{c}}$	edges	ϕ_l
$\mathcal{R}_{l\to c}$	edges	ϕ_l	primal cells	ϕ_c
$\mathcal{R}_{N\to T}$	normal components	χ_{N_l}	tangential components	χ_{T_l}
$\vec{\mathcal{R}}_{l\to c}$	normal components	χ_{N_l}	primal cells	$\boldsymbol{\chi}_c$

TABLE 3.1
List of the reconstruction operators.

given in § 3.1.3, the precise form of the reconstruction operators does not affect the main structure, nor the main properties, of the method, as far as such reconstructions are consistent. For $\mathcal{R}_{c\to l}$ we use simple averaging of $\phi_{c_{1_l}}$ and $\phi_{c_{2_l}}$, while $\mathcal{R}_{c\to\hat{c}}$, $\mathcal{R}_{l\to c}$, $\mathcal{R}_{N\to T}$ and $\vec{\mathcal{R}}_{l\to c}$ are second order accurate interpolations.

The discrete divergence and curl operators are defined as

$$\operatorname{div}(\chi_N)_c = \frac{1}{|c|} \sum_{l \in \partial c} |l| \, \mathbf{N}_l \cdot \mathbf{n}_{c,l} \, \chi_{N_l}, \quad \operatorname{div}(\chi_T)_{\hat{c}} = \frac{1}{|\hat{c}|} \sum_{\hat{l} \in \partial \hat{c}} |\hat{l}| \, \mathbf{T}_{l_{\hat{l}}} \cdot \hat{\mathbf{n}}_{\hat{c},\hat{l}} \, \chi_{T_{l_{\hat{l}}}}$$

and

$$\begin{aligned}
\operatorname{curl}(\chi_N)_{\hat{c}} &= \frac{1}{|\hat{c}|} \sum_{\hat{l} \in \partial \hat{c}} |\hat{l}| \, \mathbf{N}_{l_{\hat{l}}} \cdot \hat{\mathbf{t}}_{\hat{c},\hat{l}} \, \chi_{N_{l_{\hat{l}}}} \\
&= \frac{1}{|\hat{c}|} \sum_{\hat{l} \in \partial \hat{c}} |\hat{l}| \, \hat{\mathbf{T}}_{\hat{l}} \cdot \hat{\mathbf{t}}_{\hat{c},\hat{l}} \, \chi_{\hat{T}_{\hat{l}}}.
\end{aligned}$$

The discrete normal derivatives are defined as

$$\delta_N(\phi)_l = \frac{1}{|\hat{l}_l|} \left(\phi_{c_{2_l}} - \phi_{c_{1_l}} \right), \qquad \delta_{\hat{N}}(\phi)_{\hat{l}} = \frac{1}{|l_{\hat{l}}|} \left(\phi_{\hat{c}_{2_{\hat{l}}}} - \phi_{\hat{c}_{1_{\hat{l}}}} \right).$$

Notice that

$$\operatorname{curl}(\delta_N(\phi))_{\hat{c}} \equiv 0. \tag{3.2}$$

The differential operator associated to the diffusion term, $(\nabla \cdot (\phi \nabla \boldsymbol{\chi})) \cdot \mathbf{N}_l$, is approximated by

$$\begin{aligned}
\Delta_{\lambda,N}(\phi, \chi_N)_l = \ & -\delta_{\hat{N}} \left(\mathcal{R}_{c \to \hat{c}}(\phi) \operatorname{curl}(\chi_N) \right)_{\hat{l}_l} \\
& + \mathcal{R}_{c \to l}(\phi)_l \, \delta_N(\operatorname{div}(\chi_N))_l \\
& + \delta_N(\phi)_l \operatorname{grad}_{NN}(\chi_N)_l + \delta_{\hat{N}}(\phi)_{\hat{l}_l} \operatorname{grad}_{TN}(\chi_N)_l,
\end{aligned}$$

where the discrete gradients grad_{NN} and grad_{TN} are computed by constructing a 3rd-order least square polynomial fitting $\boldsymbol{\chi}_\lambda$ of χ_{N_l} and setting

$$\operatorname{grad}_{NN}(\chi_N)_l = \left. \frac{\partial \chi_{\lambda_N}}{\partial N} \right|_l, \quad \operatorname{grad}_{TN}(\chi_N)_l = \left. \frac{\partial \chi_{\lambda_T}}{\partial N} \right|_l.$$

Starting from $\boldsymbol{\chi}_\lambda$, we also define the cell based gradient operator

$$\operatorname{grad}(\chi_N)_c = \nabla \boldsymbol{\chi}_\lambda|_c.$$

The use of least square fitting yields a method which is robust even in the case of the unstructured spherical icosahedral grid, while the use of third order accuracy is motivated by the need of having at least second order accuracy on the components of the gradient, as it will be clear in § 3.2.

3.1.3. Space discretization. The space discretization is based on the Arakawa C-grid staggering, where the prognostic variables are the normal components of the velocity on the edges, v_{N_l}, and the free surface elevation on the primal cells, μ_c. The diagnostic variables are the absolute vorticity $\eta_{\hat{c}}$, on the dual cells, and the dynamic pressure (kinetic energy) p_{D_c} on the primal cells. To construct the space discretization, the SW-0 system (2.1) is first rewritten in invariant form as

$$\begin{aligned}
\partial_t \mu &= -\nabla \cdot (\mu \mathbf{v}) \\
\partial_t \mathbf{v} &= \eta \mathbf{v}^\perp - \nabla(g\mu + p_D) + \nu \nabla \cdot (\mu \nabla \mathbf{v}),
\end{aligned} \tag{3.3}$$

where $\eta = \mathbf{k} \cdot \nabla \times \mathbf{v} + f$ and $p_D = \frac{1}{2}|\mathbf{v}|^2$. Equation $(3.3)_1$ is discretized as

$$\partial_t \mu_c = -\operatorname{div}(\overline{\mu} \, v_N)_c, \tag{3.4}$$

where $\overline{\mu}_l = \mathcal{R}_{c \to l}(\mu)_l$. Equation $(3.3)_2$ is first multiplied by $\mathbf{N}_l$ and then discretized as

$$\partial_t v_{N_l} = \overline{\eta}_l v_{T_l} - \delta_N(g\mu + p_D)_l + \nu \Delta_{\lambda,N}(\mu, v_N)_l. \tag{3.5}$$

In (3.5), $\overline{\eta}_l = \mathcal{R}_{\hat{c} \to l}(\eta)_l$ is the reconstructed total vorticity from dual cells to edges, and the total vorticity $\eta_{\hat{c}}$ is in turn computed as

$$\eta_{\hat{c}} = \mathrm{curl}\,(v_N)_{\hat{c}} + f_{\hat{c}}.$$

As shown in [4], and as it will be also discussed in § 3.4, in order to obtain discrete conservation of potential enstrophy the reconstruction operator $\mathcal{R}_{\hat{c} \to l}$ must have the form

$$\mathcal{R}_{\hat{c} \to l}(\eta)_l = \frac{\overline{\mu}_l}{2}\left(\frac{\eta_{\hat{c}_{1_{\hat{i}_l}}}}{\mu_{\hat{c}_{1_{\hat{i}_l}}}} + \frac{\eta_{\hat{c}_{2_{\hat{i}_l}}}}{\mu_{\hat{c}_{2_{\hat{i}_l}}}}\right), \tag{3.6}$$

where $\overline{\mu}_l$ is the same reconstruction used in (3.4) and $h_{\hat{c}} = \mathcal{R}_{c \to \hat{c}}(\mu)_{\hat{c}}$. The tangential components of the velocity are obtained as $v_{T_l} = \mathcal{R}_{N \to T}(v_N)_l$. Concerning p_{D_c}, two options are available: in the first case it is computed at the edges from v_{N_l} and v_{T_l} and then interpolated on the primal cells by by means of $\mathcal{R}_{l \to c}$, while in the second case the complete velocity is first reconstructed on the primal cells through the vector valued operator $\vec{\mathcal{R}}_{l \to c}$, and then p_{D_c} is evaluated.

3.1.4. Time discretization. The system composed of (3.4) and (3.5) represents and ordinary differential equation (ODE) which, following the classical method of lines, can now be numerically integrated in time with an arbitrary time integrator. In this paper, we consider the explicit, 4th-order accurate, five stage, strongly stability preserving (SSP) Runge–Kutta (RK) scheme SSPRK(5,4) proposed in [36]. The family of SSPRK methods is widely used in computational fluid dynamics application (see for instance [15] and the references therein). The use of high order accuracy, together with the stability constraint of the explicit time discretization, results in a small error, allowing us to focus on the effects of the space discretization. In fact, in all our numerical experiments, we do not see any significant change in the solution by reducing the time-step at a fixed spatial resolution. An analysis of the trade-off between efficiency and accuracy in the choice of the time integrator is beyond the scope of this work.

We now summarize the SSPRK(5,4) algorithm. Let us first rewrite (3.4) and (3.5) in the compact form

$$\frac{dU}{dt} = \mathcal{S}(U), \tag{3.7}$$

with $U = [\mu_c, v_{N_l}]^T$ and

$$\mathcal{S}(U) = \begin{bmatrix} -\mathrm{div}\,(\overline{\mu}\,v_N)_c \\ \overline{\eta}_l v_{T_l} - \delta_N\,(g\mu + p_D)_l + \nu\Delta_{\lambda,N}\,(\mu, v_N)_l \end{bmatrix}.$$

To advance the solution from time level t^n to time level $t^{n+1} = t^n + \Delta t$ we use
- let $U^{(0)} = U^n$;
- for $i = 1, \cdots, s$ compute $U^{(i)} = \sum_{k=0}^{i-1}\left(\alpha_{ik}U^{(k)} + \Delta t \beta_{ik}\mathcal{S}(U^{(k)})\right)$;
- set $U^{n+1} = U^{(s)}$;

where $s = 5$ is the number of stages and α_{ik}, β_{ik} are suitable coefficients which are listed in Tab. 3.2. The stability region for the SSPRK(5,4) time integrator for the scalar model problem

$$\frac{dU}{dt} = \omega U, \tag{3.8}$$

with $\omega \in \mathbb{C}$, is shown in Fig. 3.1.

3.2. The α- and τ-Regularized ICON Shallow Water Model. In this section, the numerical scheme outlined in § 3.1 is extended to SW-α and SW-τ. For this purpose, we first rewrite (2.2) and (2.7) in the unified, invariant form

$$\begin{aligned} \partial_t h^\star &= -\nabla \cdot (h^\star \mathbf{u}^\star) \\ \partial_t \mathbf{u} &= \eta \mathbf{u}^{\star\perp} - \nabla\left(g\tilde{h} + p_D^\star\right) + \nu\nabla \cdot \left(\tilde{h}\nabla\mathbf{u}\right), \end{aligned} \tag{3.9}$$

α_{ik}	1.00000000000000	0	0	0	0
	0.44437049406734	0.55562950593266	0	0	0
	0.62010185138540	0	0.37989814861460	0	0
	0.17807995410773	0	0	0.82192004589227	0
	0.00683325884039	0	0.51723167208978	0.12759831133288	0.34833675773694
β_{ik}	0.39175222700392	0	0	0	0
	0	0.36841059262959	0	0	0
	0	0	0.25189177424738	0	0
	0	0	0	0.54497475021237	0
	0	0	0	0.08460416338212	0.22600748319395

TABLE 3.2

Coefficients α_{ik} and β_{ik} for the SSPRK(5,4) time integrator (see table A.2 in [36]).
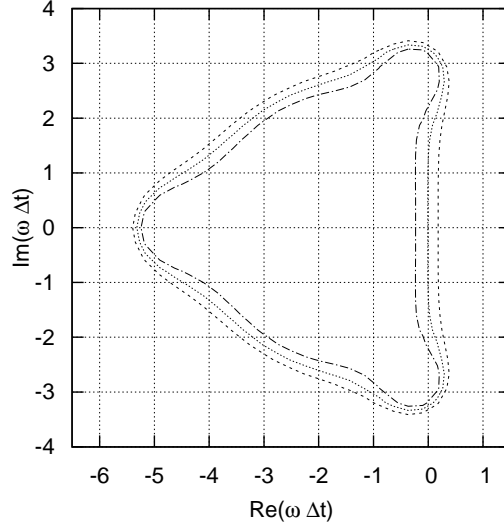
FIGURE 3.1. *Stability region for the model problem (3.8) for SSPRK(5,4) as a function of the dimensionless parameter $\omega\Delta t$. Contour lines of the absolute value of the amplification factor for amplitudes 1 (dotted line), 0.8 (dash-dotted line) and 1.2 (dashed line).*

where the meaning of the symbols $\mathbf{u}^\star$, $h^\star$ and $p_D^\star$ is summarized in Tab. 3.3. Notice that (3.9) is a generalization of (3.3). The spatial discretization of (3.9) can now proceed along the same lines of § 3.1.3, yielding the ODE system

$$\begin{aligned} \partial_t h_c^\star &= -\mathrm{div}\left(\overline{h^\star}u_N^\star\right)_c \\ \partial_t u_{N_l} &= \overline{\eta}_l u_{T_l}^\star - \delta_N\left(g\tilde{h} + p_D^\star\right)_l + \nu\Delta_{\lambda,N}\left(\tilde{h}, u_N\right)_l \end{aligned} \tag{3.10}$$

with prognostic variables $h_c^\star$ and u_{N_l}. In (3.10), $\overline{h_l^\star}$ and $\overline{\eta}_l$ are treated as in (3.4) and (3.5), respectively. Two additional diagnostic variables $\tilde{u}_{N_l}$ (for SW-α) and $\tilde{h}_c$ (for SW-τ) are introduced, obtained by solving the elliptic problems

$$\left(\overline{\tilde{h}}_l - \alpha^2\Delta_{\lambda,N}\left(\tilde{h},\cdot\right)_l\right)\tilde{u}_{N_l} = \overline{\tilde{h}}_l\,u_{N_l} \tag{3.11}$$

and

$$\left(1 - \beta^2\mathrm{div}\left(\delta_N\left(\cdot\right)\right)_c\right)\tilde{h}_c = h_c + \Pi_c, \tag{3.12}$$

where

$$\Pi_c = \begin{cases} 0 & \text{simple filtering} \\ -\frac{\beta^2}{g}\mathrm{div}\left(\overline{f}u_T^\star\right)_c & \text{filtering under linear balance} \\ -\frac{\beta^2}{g}\left(\mathrm{div}\left(\overline{\eta}u_T^\star\right)_c - \mathrm{div}\left(\delta_N\left(p_D^\star\right)\right)_c\right) & \text{filtering under nonlinear balance.} \end{cases}$$

	$\mathbf{u}^\star$	$h^\star$	$p_D^\star$
SW-α	$\tilde{\mathbf{u}}$	$\tilde{h}$	$\tilde{\mathbf{u}} \cdot \mathbf{u} - \frac{1}{2}\left(|\tilde{\mathbf{u}}|^2 + \alpha^2|\nabla\tilde{\mathbf{u}}|^2\right)$
SW-τ	$\mathbf{u}$	h	$\frac{1}{2}|\mathbf{u}|^2$

TABLE 3.3
Unified notation for SW-α and SW-τ in invariant form.

Equations (3.11) and (3.12) are the discrete counterparts of (2.3) and (2.8). Finally, for the case of SW-α, in order to compute $p_{D_c}^\star$, the complete velocities $\mathbf{u}_c$ and $\tilde{\mathbf{u}}_c$ are reconstructed on the primal cells by means of $\vec{\mathcal{R}}_{l\to c}$, as well as the complete gradient $\text{grad}\,(\tilde{\mathbf{u}})_c$, and then $p_{D_c}^\star$ is evaluated. Notice that, to obtain a consistent approximation of the gradient of $p_D^\star$, as it is required in $(3.10)_2$, at least a second order approximation of $|\nabla\tilde{\mathbf{u}}|^2$ is required.

Concerning the time discretization, the method described in § 3.1.4 can be immediately applied, upon suitable redefinition of the operator $\mathcal{S}$ according to the right hand side of (3.10). Notice that the smoothed fields $\tilde{u}_{N_l}$ and $\tilde{h}_c$ have to be diagnosed from (3.11) and (3.12) at each stage of the SSPRK(5,4). We plan to consider the possibility of freezing these variables during each RK time-step in future work.

3.3. Off-Centering of the Regularized Systems. In the pressure regularization, short wavelength gravity waves are slowed down, and, as discussed in [41] and in § 2.3, a similar effect also takes place for the velocity regularization. The slowdown of short wave modes can be problematic for the numerical approximation of SW-α and SW-τ, since for long integration times energy can accumulate in almost stationary short waves. In fact, even for moderately large integration times, the accumulation of energy at the shortest resolved wavelengths can lead to inaccurate results for the unfiltered velocity $\mathbf{u}$ and free surface elevation h. To circumvent this problem, we modify the filter operators along the lines of [37].

3.3.1. Off-centering of the SW-α system. For the case of SW-α, we substitute (2.3) with

$$\left(\tilde{h} - \alpha^2\nabla\cdot\left(\tilde{h}\nabla\right)\right)\tilde{\mathbf{u}} = \tilde{h}\left(\mathbf{u} + T_\varepsilon\left(-g\nabla\tilde{h} - f\tilde{\mathbf{u}}^\perp\right)\right), \tag{3.13}$$

where T_ε is a damping parameter having the dimension of time. Qualitatively, the additional term in the right hand side of (3.13) corresponds to extrapolating $\mathbf{u}$ from time level t to time level $t + T_\varepsilon$, since the coefficient of T_ε is, up to the nonlinear and viscous terms, the tendency of $\mathbf{u}$ in $(2.2)_2$. The resulting damping effect can be characterized by performing the dispersion analysis of the linear problem

$$\begin{aligned} \partial_t\tilde{h} &= -H_0\nabla\cdot\tilde{\mathbf{u}} \\ \partial_t\mathbf{u} &= -g\nabla\tilde{h} - f\tilde{\mathbf{u}}^\perp \\ \left(1 - \alpha^2\Delta\right)\tilde{\mathbf{u}} &= \mathbf{u} + T_\varepsilon\left(-g\nabla\tilde{h} - f\tilde{\mathbf{u}}^\perp\right), \end{aligned}$$

where H_0 is a uniform reference depth and we consider a planar geometry for simplicity. The resulting dispersion relation is

$$i\omega\left(A\,\omega^2 + B\,\omega - C\right) = 0, \tag{3.14}$$

where

$$A = 1 + T_\varepsilon^2 F, \qquad B = iT_\varepsilon\left(D + 2F\right), \qquad C = D + F,$$

and, denoting by k and l the zonal and meridional wave numbers, with $K^2 = k^2 + l^2$, we define

$$D = \frac{gH_0K^2}{1 + \alpha^2K^2}, \qquad F = \frac{f^2}{\left(1 + \alpha^2K^2\right)^2}. \tag{3.15}$$

Apart from the trivial root $\omega = 0$, corresponding to geostrophically balanced flow, a Taylor expansion for $T_\varepsilon \to 0$ gives the two roots

$$\omega_{1,2} = \pm\sqrt{D + F} - \frac{1}{2}iT_\varepsilon\left(D + 2F\right) + \mathcal{O}\left(T_\varepsilon^2\right). \tag{3.16}$$

Both frequencies in (3.16) indicate a damped solution, and for $\frac{gH_0}{f^2\alpha^2} \gg 1$, $\alpha K \geq 1$ the e-folding time is

$$\tau_\varepsilon \approx \frac{2\alpha^2}{gH_0}\frac{1}{T_\varepsilon}\left(1 + \frac{1}{\alpha^2 K^2} - 2\frac{f^2\alpha^2}{gH_0}\frac{1}{\alpha^4 K^4}\right).$$

The modification of the filter operator (3.13) is attractive for the following reasons: in contrast to the introduction of viscosity, it does not affect geostrophic flows; it has a minor impact on the numerical discretization of the problem, and in particular it does not affect the discrete conservation of potential vorticity and enstrophy, as it will be clear from § 3.4; it is similar to the divergence damping approach employed for the time regularization (see [37] and § 3.3.2), thereby simplifying comparisons of the two regularization. A drawback of (3.13) is represented by the fact that, as shown by (3.16), the damping coefficient does not vanish for $K \to 0$; the limiting value $f^2 T_\varepsilon$ however can be expected to be negligible in most of the practical applications. Concerning the discretized problem, the use of (3.13) in place of (2.3) implies that (3.11) must be modified as

$$\left(\overline{\overline{h}}_l\left(1 - T_\varepsilon f \mathcal{R}_{N\to T}\left(\cdot\right)_l\right) - \alpha^2 \Delta_{\lambda,N}\left(\tilde{h}, \cdot\right)_l\right)\tilde{u}_{N_l} = \overline{\overline{h}}_l\left(u_{N_l} - T_\varepsilon g \delta_N\left(\tilde{h}\right)_l\right). \tag{3.17}$$

3.3.2. Off-centering of the SW-τ system. For the case of SW-τ, we modify (2.8) as

$$\left(1 - \beta^2\Delta\right)\tilde{h} = h + \Pi + T_\varepsilon\left(-\nabla\cdot\left(h\mathbf{u}\right)\right), \tag{3.18}$$

where T_ε is a damping parameter. Notice the similarity between the time extrapolations in (3.18) and (3.13). The resulting damping effect can be characterized by performing the dispersion analysis of the linear problem

$$\begin{aligned}
\partial_t h &= -H_0\nabla\cdot\mathbf{u}\\
\partial_t\mathbf{u} &= -g\nabla\tilde{h} - f\mathbf{u}^\perp\\
\left(1 - \beta^2\Delta\right)\tilde{h} &= h - \mathcal{B}\beta^2\frac{f}{g}\nabla\cdot\mathbf{u}^\perp - T_\varepsilon H_0\nabla\cdot\mathbf{u},
\end{aligned}$$

where $\mathcal{B} = 0$ corresponds to simple filtering and $\mathcal{B} = 1$ corresponds to filtering under linear balance. The resulting dispersion relation is

$$i\omega\left(\omega^2 + B\omega - C\right) = 0, \tag{3.19}$$

where

$$B = iT_\varepsilon P, \qquad C = P + Q,$$

and we define

$$P = \frac{gH_0 K^2}{1 + \beta^2 K^2}, \qquad Q = \frac{1 + (1 - \mathcal{B})\beta^2 K^2}{1 + \beta^2 K^2}f^2. \tag{3.20}$$

Apart from the trivial root $\omega = 0$, corresponding to geostrophically balanced flow, a Taylor expansion for $T_\varepsilon \to 0$ gives the two roots

$$\omega_{1,2} = \pm\sqrt{P + Q} - \frac{1}{2}iT_\varepsilon D + \mathcal{O}\left(T_\varepsilon^2\right). \tag{3.21}$$

Both frequencies in (3.16) indicate a damped solution with e-folding time

$$\tau_\varepsilon = \frac{2\beta^2}{gH_0}\frac{1}{T_\varepsilon}\left(1 + \frac{1}{\beta^2 K^2}\right),$$

which can be immediately compared to the e-folding time derived in § 3.3.1 for SW-α.

3.4. Discrete Conservation of Potential Vorticity and Enstrophy. In this section, it is shown how the spatial discretization (3.10) results, for the inviscid case, in the discrete conservation of potential vorticity and enstrophy. The presentation closely follows § 6 of [4]; we omit the superscipt in $h^\star$ for simplicity. First of all, we need to introduce a discrete continuity equation on the dual grid, given by

$$\partial_t \hat{h}_{\hat{c}} = -\mathrm{div}\left(\overline{h} u_T^\star\right)_{\hat{c}}. \tag{3.22}$$

In (3.22), $\overline{h}_{\hat{l}_l}$ and $u_{T_{\hat{l}_l}}^\star$ are the same as in $(3.10)_1$ and $(3.10)_2$, respectively, while $\hat{h}_{\hat{c}}$ is an approximation of the free surface height on the dual cells which is initialized as $\hat{h}_{\hat{c}}(0) = \mathcal{R}_{c\to\hat{c}}\left(h\right)_{\hat{c}}(0)$ at the initial time level and then evolved according to (3.22). Notice that, in general, we have $\hat{h}_{\hat{c}} \neq \mathcal{R}_{c\to\hat{c}}\left(h\right)_{\hat{c}}$ for time levels different from the initial one. We now take the discrete curl of $(3.10)_2$, assume $\nu = 0$ and use (3.2), obtaining

$$\partial_t \left(\mathrm{curl}\left(u_N\right)_{\hat{c}}\right) = -\mathrm{div}\left(\overline{\eta} u_T^\star\right)_{\hat{c}}. \tag{3.23}$$

If the potential vorticity is now defined on the dual grid as

$$q_{\hat{c}} = \frac{\mathrm{curl}\left(u_N\right)_{\hat{c}} + f}{\hat{h}_{\hat{c}}}$$

and the edge-averaged potential vorticity is given by $\overline{q}_l = \overline{\eta}_l / \overline{h}_l$, from (3.23) follows

$$\partial_t \left(q_{\hat{c}} \, \hat{h}_{\hat{c}}\right) = -\mathrm{div}\left(\overline{q}\overline{h} \, u_T^\star\right)_{\hat{c}}, \tag{3.24}$$

which, combined with (3.22), provides discrete conservation of $q_{\hat{c}}$. In particular, we have

$$\sum_{\hat{c}\in\mathscr{D}_\lambda} q_{\hat{c}} \, \hat{h}_{\hat{c}} = \sum_{\hat{c}\in\mathscr{D}_\lambda} \eta_{\hat{c}} = const. \tag{3.25}$$

REMARK 3.1. *Notice that the second equality in (3.25) follows immediately from (3.23). The introduction of $\hat{h}_{\hat{c}}$, $q_{\hat{c}}$ and (3.24) represents simply a rephrasing of (3.23). More subtle is, however, the issue of potential enstrophy conservation.*

To obtain a discrete conservation equation for the potential enstrophy, we first notice that, thanks to (3.22) and (3.24),

$$\hat{h}_{\hat{c}} \, \partial_t q_{\hat{c}} = \partial_t \left(q_{\hat{c}} \, \hat{h}_{\hat{c}}\right) - q_{\hat{c}} \, \partial_t \hat{h}_{\hat{c}} = -\mathrm{div}\left(\overline{q}\overline{h} \, u_T^\star\right)_{\hat{c}} + q_{\hat{c}}\mathrm{div}\left(\overline{h} u_T^\star\right)_{\hat{c}}. \tag{3.26}$$

Hence, we have

$$
\begin{aligned}
\partial_t \left(q_{\hat{c}}^2 \, \hat{h}_{\hat{c}}\right) &= q_{\hat{c}}^2 \, \partial_t \hat{h}_{\hat{c}} + 2q_{\hat{c}} \, \hat{h}_{\hat{c}} \, \partial_t q_{\hat{c}} \\
&= -q_{\hat{c}}^2 \mathrm{div}\left(\overline{h}u_T^\star\right)_{\hat{c}} - 2q_{\hat{c}}\mathrm{div}\left(\overline{q}\overline{h}\,u_T^\star\right)_{\hat{c}} + 2q_{\hat{c}}^2\mathrm{div}\left(\overline{h}u_T^\star\right)_{\hat{c}} \\
&= q_{\hat{c}}^2 \mathrm{div}\left(\overline{h}u_T^\star\right)_{\hat{c}} - 2q_{\hat{c}}\mathrm{div}\left(\overline{q}\overline{h}\,u_T^\star\right) \\
&= -\frac{1}{|\hat{c}|}\sum_{\hat{l}\in\partial\hat{c}} |\hat{l}|\, \mathbf{T}_{l_{\hat{l}}} \cdot \hat{\mathbf{n}}_{\hat{c},\hat{l}} \, \overline{h}_{l_{\hat{l}}} u_{T_{l_{\hat{l}}}}^\star \left(2q_{\hat{c}}\overline{q}_{l_{\hat{l}}} - q_{\hat{c}}^2\right)
\end{aligned} \tag{3.27}
$$

For (3.27) to represent a discrete balance equation, the term $\left(2q_{\hat{c}}\overline{q}_{l_{\hat{l}}} - q_{\hat{c}}^2\right)$ must be single valued on $\hat{l}$, or

$$2q_{\hat{c}_{1_{\hat{l}}}}\overline{q}_{l_{\hat{l}}} - q_{\hat{c}_{1_{\hat{l}}}}^2 = 2q_{\hat{c}_{2_{\hat{l}}}}\overline{q}_{l_{\hat{l}}} - q_{\hat{c}_{2_{\hat{l}}}}^2$$

which can be solved in $\overline{q}_{l_{\hat{l}}}$ to obtain

$$\overline{q}_{l_{\hat{l}}} = \frac{q_{\hat{c}_{1_{\hat{l}}}} + q_{\hat{c}_{2_{\hat{l}}}}}{2}. \tag{3.28}$$

Averaging (3.28) in turns implies

$$\overline{\eta}_l = \frac{\overline{h}_l}{2}\left(\frac{\eta_{\hat{c}_{1_{\hat{i}_l}}}}{\hat{h}_{\hat{c}_{1_{\hat{i}_l}}}} + \frac{\eta_{\hat{c}_{2_{\hat{i}_l}}}}{\hat{h}_{\hat{c}_{2_{\hat{i}_l}}}}\right), \tag{3.29}$$

which is analogous to (3.6) except for the use of $\hat{h}_{\hat{c}}$ in place of $h_{\hat{c}}$. As a consequence of (3.27) and (3.28), one has

$$\sum_{\hat{c}\in\mathscr{D}_\lambda} q_{\hat{c}}^2\,\hat{h}_{\hat{c}} = \sum_{\hat{c}\in\mathscr{D}_\lambda} \frac{\eta_{\hat{c}}^2}{\hat{h}_{\hat{c}}} = const. \tag{3.30}$$

REMARK 3.2. *While the introduction of $\hat{h}_{\hat{c}}$ and the associated prognostic equation (3.22) has no practical impact on (3.25), as noted in remark 3.1, it does have an impact on (3.30). In fact, $\hat{h}_{\hat{c}}$ must be known in order to compute $\overline{\eta}_l$ in (3.29). In practice, however, the prognostic equation (3.22) is not solved, since it would result in a drift between h_c and $\hat{h}_{\hat{c}}$, each of which is independently obtained from a prognostic equation, and (3.6) is used instead of (3.29). As a consequence, Eq. (3.30) is not exactly satisfied.*

4. Numerical Results. In this section, a numerical validation of the proposed discretization of the velocity and pressure regularized equations is presented, with two main purposes: assess the stability properties of the resulting numerical scheme and analyze the impact of the regularizations on the computed solution. For each test case, we provide results for SW-α and SW-τ as well as for explicit integrations of the unfiltered SW-0 system which serves as a reference. Stability is studied considering the size of the maximum allowable Courant number and the amount of off-centering required in the computation; the effect of the regularization is analyzed by comparing the computed solutions and by verifying that the observed differences are consistent with what is expected for the continuous problem on the basis of the discussion of § 2, rather than being an artifact of the numerical discretization. The time evolution of the total energy and enstrophy is also diagnosed, while we do not show results for the mass and vorticity conservations since these quantities are always conserved up to machine precision by our method. The considered test cases are two-dimensional and the geometry is either planar, with uniform Coriolis parameter (f-plane) and periodic boundary conditions, or spherical. The computational domain for the f-plane tests of § 4.1, § 4.2 and § 4.4 is is the rectangle $[0\,,L_x]\times[0\,,L_y]$, with $L_x = 5000\,km$, $L_y = 4330\,km$, and we set $f = 6.147\cdot10^{-5}\,s^{-1}$, which corresponds to a latitude of 25°. The grid is structured and composed of equilateral triangles. For the Rossby-Haurwitz wave test of § 4.3 the computational domain is the sphere of radius $R_{Earth} = 6.371\cdot10^3\,km$ and angular velocity $\Omega_{Earth} = 7.292\cdot10^{-5}s^{-1}$. In this case, an icosahedral triangular grid is used [4]. For all the runs, the time integration is performed with the SSPRK(5,4) method summarized in § 3.1.4. Consistently with § 2.3, a unique, prescribed initial condition is used to initialize SW-0, SW-τ and the velocity field of SW-α, while $\tilde{h}$ in this latter model is initialized with a smoothed free surface elevation profile.

4.1. Vortex pair interaction. For the first test case, we consider the vortex pair problem described in [33, 38, 34], where the time evolution of two interacting, corotating vortices is studied in the inviscid case. The initial condition is prescribed through the free surface elevation and the constraint of geostrophic balance, and the time integration is carried out up to $T^{fin} = 10\,days$. More in details, we set

$$\begin{aligned}
h(x,y,0) &= H_0 - H'\left[e^{-\frac{1}{2}\left(x_1'^2+y_1'^2\right)} + e^{-\frac{1}{2}\left(x_2'^2+y_2'^2\right)} - \frac{4\pi\sigma_x\sigma_y}{L_xL_y}\right], \\
u(x,y,0) &= -\frac{gH'}{f\sigma_y}\left[y_1''e^{-\frac{1}{2}\left(x_1'^2+y_1'^2\right)} + y_2''e^{-\frac{1}{2}\left(x_2'^2+y_2'^2\right)}\right], \\
v(x,y,0) &= +\frac{gH'}{f\sigma_x}\left[x_1''e^{-\frac{1}{2}\left(x_1'^2+y_1'^2\right)} + x_2''e^{-\frac{1}{2}\left(x_2'^2+y_2'^2\right)}\right],
\end{aligned} \tag{4.1}$$

with

$$x'_{1,2} = \frac{L_x}{\pi \sigma_x} \sin\left(\frac{\pi}{L_x}\left(x - x_{c_{1,2}}\right)\right), \quad y'_{1,2} = \frac{L_y}{\pi \sigma_y} \sin\left(\frac{\pi}{L_y}\left(y - y_{c_{1,2}}\right)\right),$$

$$x''_{1,2} = \frac{L_x}{2\pi \sigma_x} \sin\left(\frac{2\pi}{L_x}\left(x - x_{c_{1,2}}\right)\right), \quad y''_{1,2} = \frac{L_y}{2\pi \sigma_y} \sin\left(\frac{2\pi}{L_y}\left(y - y_{c_{1,2}}\right)\right).$$

In our experiment we use

$$x_{c_1} = \left(\tfrac{1}{2} - o\right) L_x, \quad x_{c_2} = \left(\tfrac{1}{2} + o\right) L_x, \quad \sigma_x = \tfrac{3}{40} L_x,$$

$$y_{c_1} = \left(\tfrac{1}{2} - o\right) L_y, \quad y_{c_2} = \left(\tfrac{1}{2} + o\right) L_y, \quad \sigma_y = \tfrac{3}{40} L_y,$$

and $o = 0.1$. Figure 4.1 illustrates the initial surface elevation and relative potential vorticity $q - f/h = |\nabla \times \mathbf{u}|/h$. In order to characterize the flow resulting from (4.1), we now consider a set of dimensionless
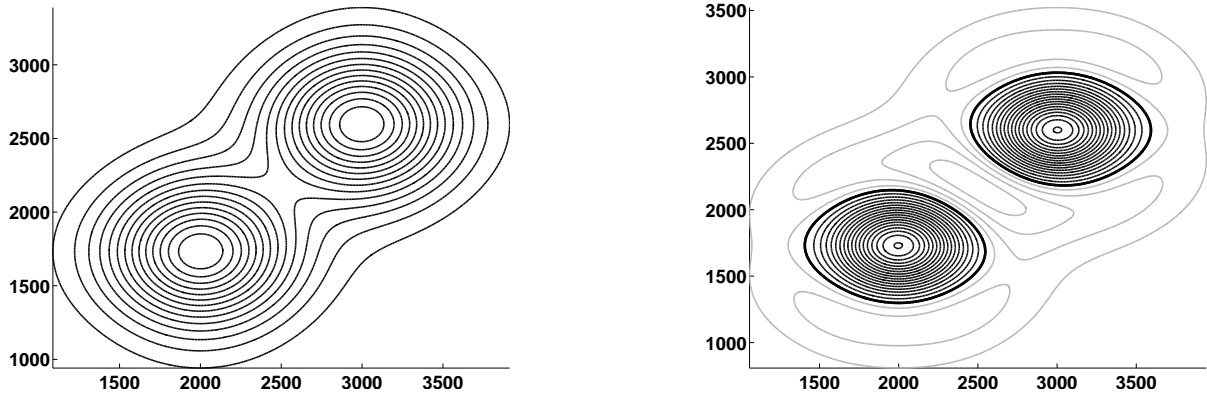
FIGURE 4.1. *Vortex pair test case with $H_0 = 10000\,m$, initial condition (axes in km). Layer depth pertubation, $h - H_0$, left, contours between $-70\,m$ and $0\,m$, contour interval of $5\,m$. Relative potential vorticity, right, contours between $-0.45\,days^{-1}km^{-1}$ and $1.7\,days^{-1}km^{-1}$, contour interval of $0.1\,days^{-1}km^{-1}$ (negative values in gray, positive values in black, zero contour thicker).*

parameter. To this end, since $\sigma_x \approx \sigma_y$, we can define the characteristic length scale $d = 4\sigma$, with $\sigma = \frac{1}{2}(\sigma_x + \sigma_y)$ and obtain the characteristic velocity U and characteristic time T as

$$U = 2\frac{gH'}{fd}, \qquad T = \frac{d}{U} = \frac{1}{2}\frac{fd^2}{gH'}.$$

The resulting Froude, Rossby and Burger numbers are

$$F = \frac{U}{\sqrt{gH_0}} = 2\frac{\sqrt{gH'}}{fd}\sqrt{\frac{H'}{H_0}}, \qquad R = \frac{U}{fd} = 2\frac{gH'}{f^2d^2}, \qquad B \equiv \frac{R^2}{F^2} = \frac{L_D^2}{d^2} = \frac{gH_0}{f^2d^2},$$

where $L_D = \frac{\sqrt{gH_0}}{f}$ is the Rossby deformation radius. As discussed in [30], Chap. 3.12, the flow is in geostrophic regime for $R \ll 1$, or $H' \ll \frac{1}{2}\frac{f^2d^2}{g}$. Among geostrophic flows, we can further distinguish the *semi-geostrophic* regime, for $B \ll 1$, the *quasi-geostrophic* regime, for $B \approx 1$, and the *incompressible* regime for $B \gg 1$ (see for instance [7]). Concerning the Froude number, we notice that it provides an indication of the ratio between the explicit and the semi-implicit stable time steps. This analysis indicates that geostrophically balanced flows with different Burger numbers, and hence different degrees of compressibility, can be obtained by varying H_0, and in particular divergence free flows correspond to $H_0 \to \infty$. We thus fix $H' = 75\,m$ and consider the three cases $H_0 = 450\,m$, which is in the semi-geostrophic regime, $H_0 = 750\,m$, corresponding to the quasi-geostrophic regime, and $H_0 = 10000\,m$, where the flow is almost incompressible. The resulting characteristic scales are summarized in Tab. 4.1. The numerical setup is given by a grid of 256 rows, each row consisting of 256 upward pointing triangles

	$H_0 = 450\,m$	$H_0 = 750\,m$	$H_0 = 10000\,m$
d	$1.40 \cdot 10^3\,km$	$1.40 \cdot 10^3\,km$	$1.40 \cdot 10^3\,km$
U	$17.1\,ms^{-1}$	$17.1\,ms^{-1}$	$17.1\,ms^{-1}$
T	$0.947\,days$	$0.947\,days$	$0.947\,days$
L_D	$1.08 \cdot 10^3\,km$	$1.40 \cdot 10^3\,km$	$5.10 \cdot 10^3\,km$
F	0.257	0.199	0.055
R	0.199	0.199	0.199
B	0.596	0.994	13.26

TABLE 4.1

Characteristic scales and dimensionless numbers for the vortex pair test case for three different choices of H_0 in (4.1), corresponding to semi-geostrophic, quasi-geostrophic and incompressible flows, respectively.

and the same number of downward pointing triangles, so that the domain consists of a total of $2 \cdot 256^2 = 131072$ triangles. Hence, the spatial resolution, defined as the edge length of a triangle, is $\lambda = 19.5\,km$. The time step of SW-0 is determined by setting the Courant number $C = \Delta t \sqrt{gH_0}/\lambda$ to the rather conservative value 0.5, while for SW-α and SW-τ we use the maximum time step allowed by the velocity and pressure regularizations. For ease of comparison, we set $\alpha = \beta$, and the resulting time steps are summarized in Tab. 4.2. No off-centering is used for any of the regularized models. As expected, both

	$H_0 = 10000\,m$	$H_0 = 750\,m$	$H_0 = 450\,m$
λ	$19.5\,km$	$19.5\,km$	$19.5\,km$
$\sqrt{gH_0}$	$313\,ms^{-1}$	$85.8\,ms^{-1}$	$66.4\,ms^{-1}$
α	$95.8\,km$	$26.0\,km$	$20.3\,km$
β	$95.8\,km$	$26.0\,km$	$20.3\,km$
α/λ	4.9	1.3	1.04
β/λ	4.9	1.3	1.04
Δt_0	$30\,s$	$120\,s$	$150\,s$
Δt_α	$540\,s$	$540\,s$	$570\,s$
Δt_τ	$600\,s$	$600\,s$	$600\,s$

TABLE 4.2

Summary of the main parameters used in the vortex pair experiments for various flow regimes. Δt_0, Δt_α and Δt_τ are the time steps used in SW-0, SW-α and SW-τ, respectively.

models, SW-α and SW-τ, allow time steps which are larger than the stable explicit one and almost independent from the velocity of the gravity waves. Moreover, for a fixed smoothing length, the stable time step for SW-τ is found to be slightly larger than for SW-α.

The surface elevation and the relative potential vorticity of the computed solutions at time T^{fin} are plotted in Figs. 4.2-4.4. An overall agreement of the three models can be observed in all the considered flow regimes. The potential vorticity plots are essentially undistinguishable, while from the plots of the free surface elevation it can be seen that both SW-α and SW-τ result in a similar pattern for $1000\,km < y < 3000\,km$, which is different from SW-0 and which is associated with a modified propagation of the gravity waves. Since the scale separation between gravity waves and advection decreases with increasing Froude number, this effect is less observable in Fig. 4.4.   The evolution in time of the energy and enstrophy integrals is represented in Fig. 4.5 for the incompressible case. It can be seen that the integration of the regularized models yields very small relative energy and enstrophy deviations of the order of 10^{-6}. Within this range, rather a decay of energy and enstrophy than a growth can be observed, which is expected to be beneficial for the stability of the method. Analogous results are obtained in the other two regimes.

4.2. Shear flow evolution. In the second test case, the evolution of a shear flow is considered. The initial condition is prescribed through the free surface elevation and the constraint of geostrophic
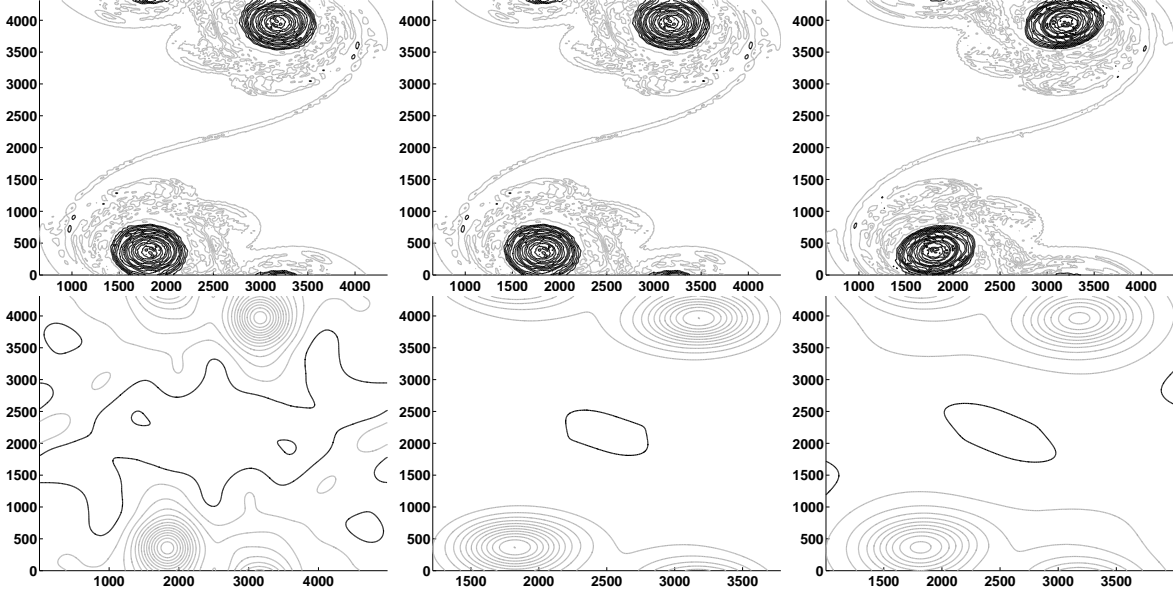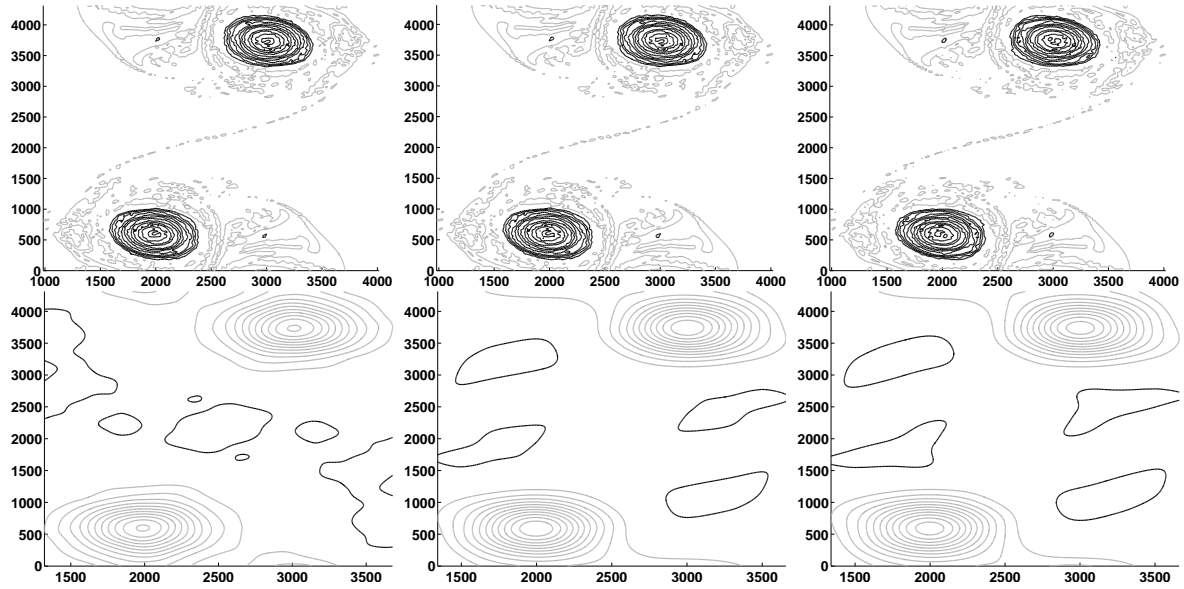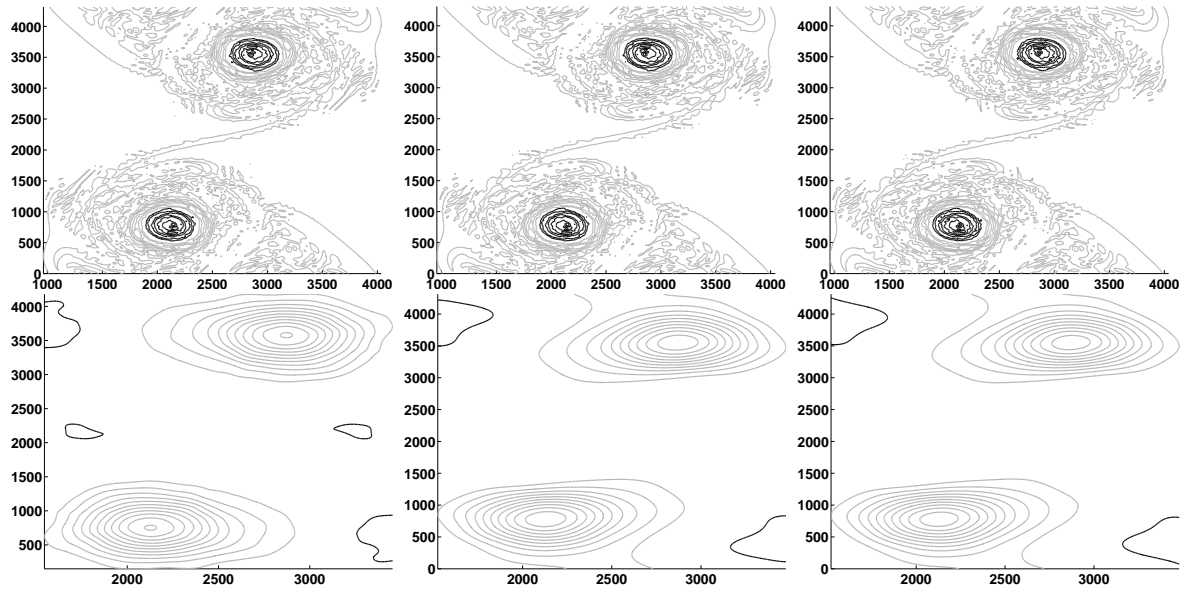
FIGURE 4.2. *Vortex pair test case with $H_0 = 10000\,m$ at time $10\,days$. Upper row: relative potential vorticity, contours between $-0.7\,days^{-1}km^{-1}$ and $1.9\,days^{-1}km^{-1}$ with contour interval of $0.1\,days^{-1}km^{-1}$ (negative values in gray, positive values in black, zero contour line omitted), results for SW-0, left, SW-τ, center, and SW-α, right. Bottom row: surface elevation $h - H_0$, contours between $-120\,m$ and $20\,m$ with contour interval $10\,m$, results for SW-0, SW-τ and SW-α as above.*

balance. More in details, we set

$$
\begin{aligned}
h(x,y,0) &= H_0 - H' \frac{y''}{\sigma_y} e^{-\frac{y'^2}{2\sigma_y^2}+\frac{1}{2}} \left(1 + \kappa \sin\left(\frac{2\pi x'}{\lambda_x}\right)\right), \\
u(x,y,0) &= \frac{gH'}{\sigma_y f L_y} \left(c(y) - \frac{y''^2}{\sigma_y^2}\right) e^{-\frac{y'^2}{2\sigma_y^2}+\frac{1}{2}} \left(1 + \kappa \sin\left(\frac{2\pi x'}{\lambda_x}\right)\right), \\
v(x,y,0) &= -\frac{gH'}{f L_x} \frac{2\pi\kappa}{\lambda_x} \frac{y''}{\sigma_y} e^{-\frac{y'^2}{2\sigma_y^2}+\frac{1}{2}} \cos\left(\frac{2\pi x'}{\lambda_x}\right),
\end{aligned}
\tag{4.2}
$$

with $x' = \frac{x}{L_x}$ and $c(y) = \cos\left(\frac{2\pi}{L_y}\left(y - \frac{L_y}{2}\right)\right)$,

$$
y' = \frac{1}{\pi}\sin\left(\frac{\pi}{L_y}\left(y - \frac{L_y}{2}\right)\right), \quad y'' = \frac{1}{2\pi}\sin\left(\frac{2\pi}{L_y}\left(y - \frac{L_y}{2}\right)\right),
$$

$\lambda_x = \frac{1}{2}$, $\sigma_y = \frac{1}{12}$ and $\kappa = 0.1$. The characteristic lengths of the problem are $\lambda_x L_x$ in the zonal direction and $4\sigma_y L_y$ in the meridional direction. Noting that these two scales are similar, we can choose $d = 4\sigma_y L_y$ as reference length of the problem. The characteristic velocity and time scales are then

$$
U = 6\frac{gH'}{fd}, \qquad T = \frac{d}{U} = \frac{1}{6}\frac{fd^2}{gH'},
$$

while the Froude, Rossby and Burger numbers are

$$
F = 6\frac{\sqrt{gH'}}{fd}\sqrt{\frac{H'}{H_0}}, \qquad R = 6\frac{gH'}{f^2 d^2}, \qquad B = \frac{gH_0}{f^2 d^2}.
$$

Upon setting $H_0 = 1076\,m$ and $H' = 30\,m$, we obtain the characteristic scales listed in Tab. 4.3. The flow is in the quasi-geostrophic regime, and it is inviscid. The numerical setup is as follows. The computational grid described in § 4.1 is used and the smoothing length is $30\,km$ for both SW-α and

FIGURE 4.3. *Vortex pair test case with $H_0 = 750\,m$ at time $10\,days$. Upper row: relative potential vorticity, contours between $-8\,days^{-1}km^{-1}$ and $26\,days^{-1}km^{-1}$ with contour interval of $2\,days^{-1}km^{-1}$ (negative values in gray, positive values in black, zero contour line omitted), results for SW-0, left, SW-τ, center, and SW-α, right. Bottom row: surface elevation $h - H_0$, contours between $-120\,m$ and $20\,m$ with contour interval $10\,m$, results for SW-0, SW-τ and SW-α as above.*

FIGURE 4.4. *Vortex pair test case with $H_0 = 450\,m$ at time $10\,days$. Upper row: relative potential vorticity, contours between $-13\,days^{-1}km^{-1}$ and $50\,days^{-1}km^{-1}$ with contour interval of $3\,days^{-1}km^{-1}$ (negative values in gray, positive values in black, zero contour line omitted), results for SW-0, left, SW-τ, center, and SW-α, right. Bottom row: surface elevation $h - H_0$, contours between $-120\,m$ and $20\,m$ with contour interval $10\,m$, results for SW-0, SW-τ and SW-α as above.*

SW-τ. Concerning the time step, while the Courant–Friedrichs–Lewy condition for SW-0 results in a time step of $120\,s$, a significantly larger time step can be used with SW-α and SW-τ, namely $480\,s$ for SW-α and $600\,s$ for SW-τ. No off-centering is applied to any of the regularized systems.

The evolution of the flow up to day 10 is represented for SW-0 in Fig. 4.6, where the relative potential vorticity is plotted. Qualitatively similar results are obtained for SW-α and SW-τ. It can be
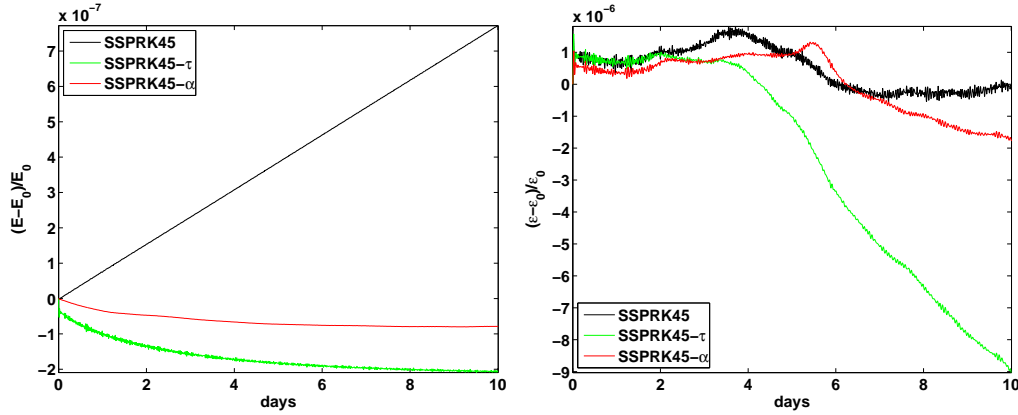
FIGURE 4.5. *Vortex pair test case with $H_0 = 10000\,m$: relative deviations of energy (left) and enstrophy (right) during the time integration for SW-0 (black, label "SSPRK45"), SW-τ (red, label "SSPRK45-τ") and SW-α (green, label "SSPRK45-α").*

d	$1.44 \cdot 10^3\,km$
U	$19.9\,ms^{-1}$
T	$0.839\,days$
L_D	$1.67 \cdot 10^3\,km$
F	0.194
R	0.224
B	1.34

TABLE 4.3
Characteristic scales and dimensionless number for the shear flow test case.

seen that the perturbation superimposed on the initial zonal jet grows in amplitude, and a dominant, wave number two component is clearly visible at day 3. The instability evolves in two couples of counter-rotating vortices, which can be seen at day 6, and by day 10 the whole domain is occupied by the vortical motion. At this point, the vorticity filaments have reached scales that are beyond the spatial resolution of the grid. For a discussion of the results, we present plots of the displacement of the free surface
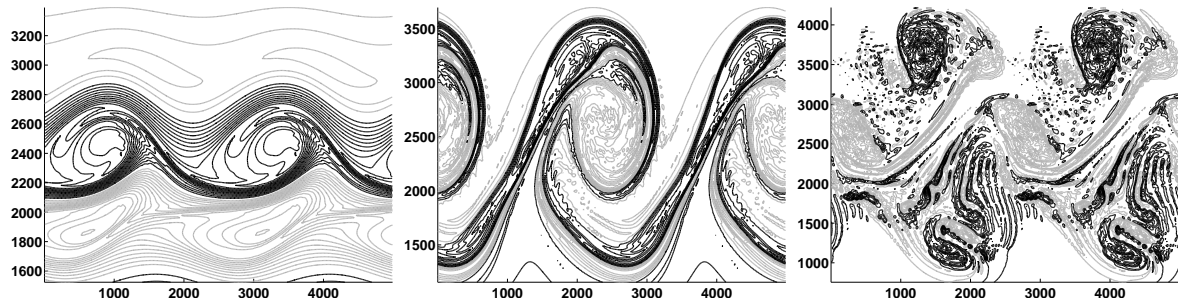
FIGURE 4.6. *Shear flow test case, relative potential vorticity at days 3 (left), 6 (center) and 10 (right). Contours between $-11\,days^{-1}km^{-1}$ and $12\,days^{-1}km^{-1}$ with contour interval of $0.5\,days^{-1}km^{-1}$. Axis in km, notice that the limits of the y axis are adjusted in each plot to the region of the domain interested by the flow.*

height for days 3, 6 and 10 in Fig. 4.7. From this figure, we conclude first of all that SW-0, SW-α and SW-τ yield similar results, the maximum difference in free surface height being 0.3%. We also note that SW-α and SW-τ affect in a very similar way the propagation of the gravity waves, as it can be seen from the analogous patterns that are present for $y \leq 1500\,km$ and $y \geq 3500\,km$ in the center and right panels of Fig. 4.7. In addition, SW-α also determines a phase shift in the position of the resulting vortices, which can be seen for $1500 < y < 3500$ in the right panel of Fig. 4.7 and is particularly evident

at day 6. This is a consequence of the modified advection term and of the presence of flow features with spatial scale comparable to α. In order to assess the extent to which the conservation properties
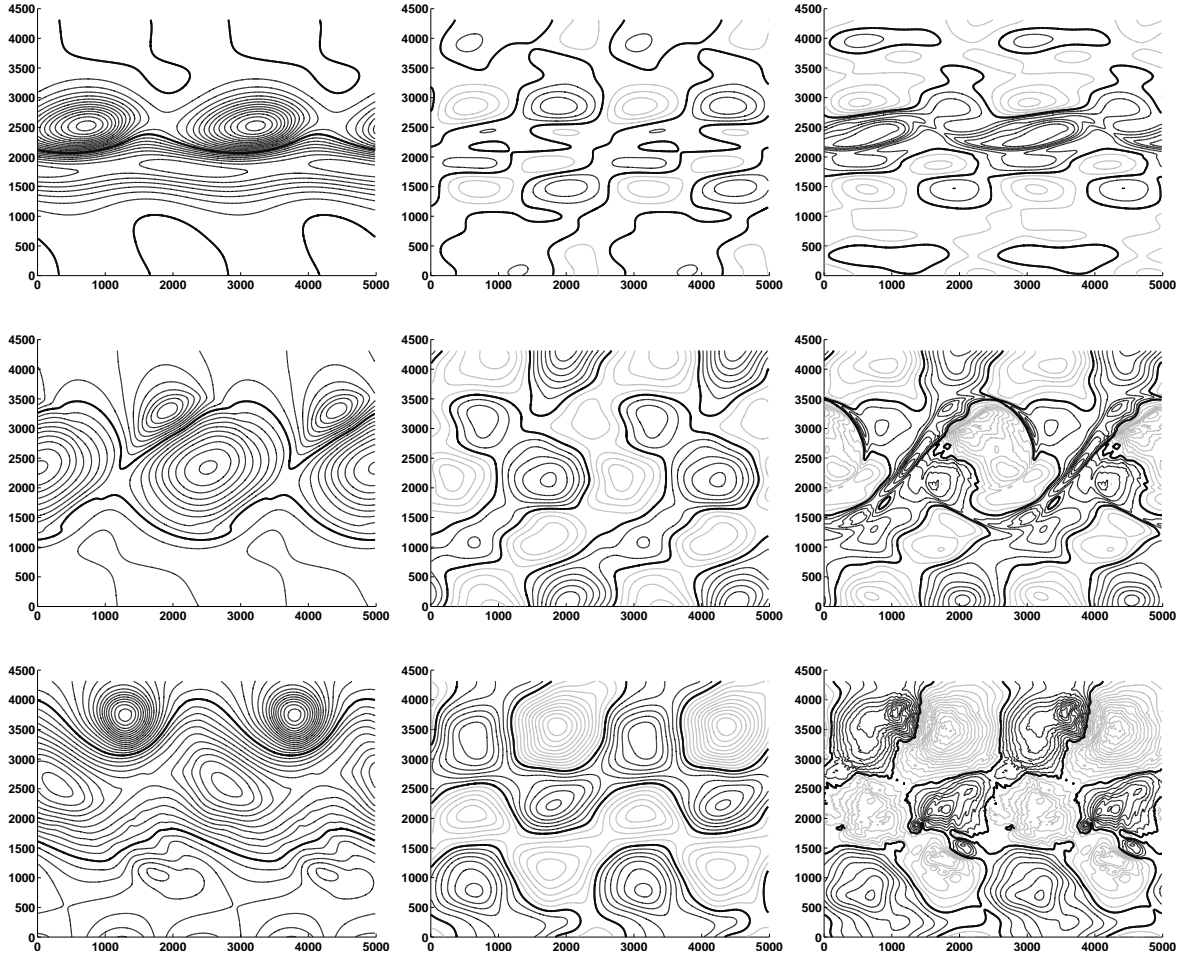

FIGURE 4.7. *Shear flow test case, displacement of the free surface elevation $h - H_0$. The plots are organized so that the first, second and third row corresponds to time level $3\,days$, $6\,days$ and $10\,days$, respectively, while the first, second and third column corresponds to SW-0, relative difference between SW-τ and SW-0 and relative difference between SW-α and SW-0, respectively. In the first column the contours range from $-60\,m$ to $40\,m$ with contour intervals of $4\,m$, while in the second and third columns contours between -0.003 and 0.003 with contour interval $2 \cdot 10^{-4}$ are used. Axis in km, gray lines for negative values, black lines for positive values and thicker line for the zero level.*

of the continuous problem are preserved by the numerical scheme, a 100 day integration has also been performed, well beyond the time at which the flow starts to develop unresolved features. The relative variations of total energy and potential enstrophy for this run are plotted in Fig. 4.8, where it can be seen that these quantities are preserved for all the considered models up to relative deviations of the order 10^{-7} for energy and 10^{-5} for potential enstrophy. A detail of the evolution of two components of the total energy, namely the potential energy and, only for the SW-α system, the gradient kinetic energy (see (2.5))

$$E_{\alpha,\nabla} = \frac{1}{2} \int_\Omega \alpha^2 \tilde{h} |\nabla \tilde{\mathbf{u}}|^2 d\mathbf{x},$$

is provided in Fig. 4.9. Notice that $E_{\alpha,\nabla}$ is the complement to the complete kinetic energy of the velocity component

$$E_{\alpha,\mathbf{u}} = \frac{1}{2} \int_\Omega \tilde{h} |\tilde{\mathbf{u}}|^2 d\mathbf{x}.$$
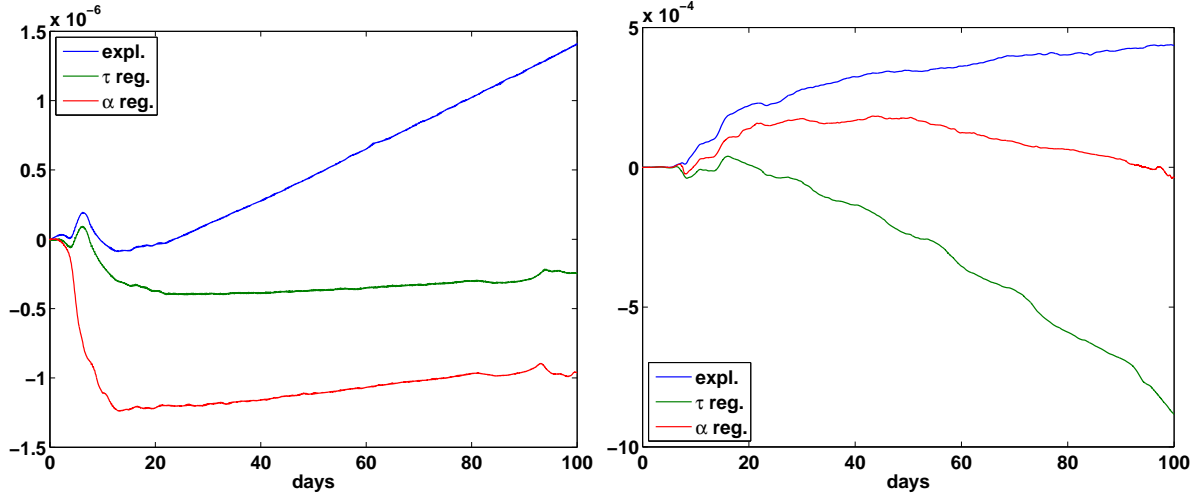
FIGURE 4.8. *Shear flow test case, relative variations of the total energy (left) and potential enstrophy (right) during a long time integration for SW-0, blue, SW-τ, green and SW-α, red.*

Here, it can be seen that the gradient kinetic energy exhibits variations which are approximately one fourth of those of the potential energy (which are, in turn, of the same order of the variations of the kinetic energy). This fact shows that a proper representation of $E_{\alpha,\nabla}$ in the model is essential in order to close the energy balance. It should also be noted that $E_{\alpha,\nabla}$ *decreases* during the integration. This is a very general characteristic of all our experiments, and is in stark contrast with what is reported in [27], Sect. IV, where the initial transient is characterized by an *increase* of the gradient kinetic energy. In comparing our results with [27], however, we have to consider that in this latter work a three dimensional experiment is considered, and the increase of the gradient term indicates an increase in enstrophy. On the other hand, in our two dimensional test enstrophy is almost constant.
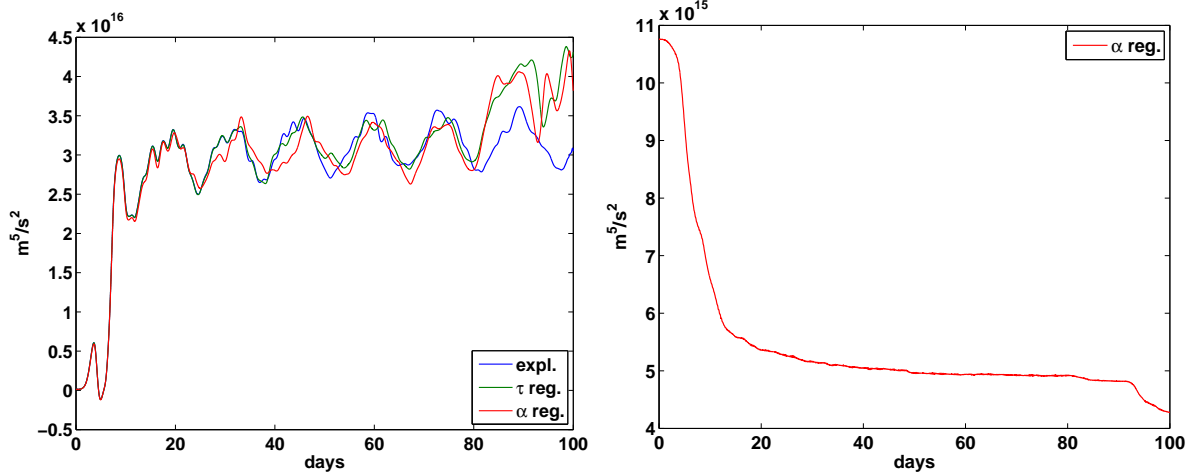
FIGURE 4.9. *Shear flow test case, detail of the energy evolution during a long time integration. Left: potential energy for SW-0, blue, SW-τ, green and SW-α, red. Right: gradient kinetic energy for the SW-α model. For visualization purposes a low pass filter with cut-off frequency corresponding to 0.5 days has been applied to filter the gravity waves in the plots of the potential energy.*

4.2.1. Development of the shear instability in the regularized models. As shown in [21], the use of a regularized set of equation can modify the stability properties of the flow, shifting the onset of the instability. To verify the effect of the velocity and pressure regularizations on the instability of the shear flow, we compare in the present section various experiments with varying regularization

parameters. More in details, we consider the test case (4.2) and we reduce the initial disturbance by setting $\kappa = 0.025$. A mesh size $\lambda = 78.125\,km$, which corresponds to $2 \cdot 64^2 = 8192$ triangles, is considered. A qualitative indication of the onset of the instability is provided by the maximum value of the meridional velocity, which is negligible in the initial condition and reaches a value of approximately $20\,ms^{-1}$ after the formation of the four vortices. Figure 4.10, left, shows the value of the maximum meridional velocity for the following cases: SW-0, SW-τ with $\Delta t = 30\,min$, corresponding to a smoothing length of $94.17\,km$, and the space regularized SW equations with α equal to $63\,km$, $126\,km$, $188\,km$, $251\,km$, $314\,km$ and $377\,km$, with $\Delta t = 16\,min$ for $\alpha = 63\,km$ (dictated by the gravity wave CFL condition) and $\Delta t = 32\,min$ for the other cases (dictated by the advective CFL condition). For the cases with $\alpha \geq 251\,km$ an off-centering has also been used with $T_\varepsilon = 11\,s$ in (3.13). From this picture it is clear that the two regularizations have a different impact on the onset of the instability: the pressure regularization does not affect the large scale instability, which is, on the contrary, delayed by the velocity regularization. Figure 4.10, right, shows the time evolution of the kinetic energy contributions for the
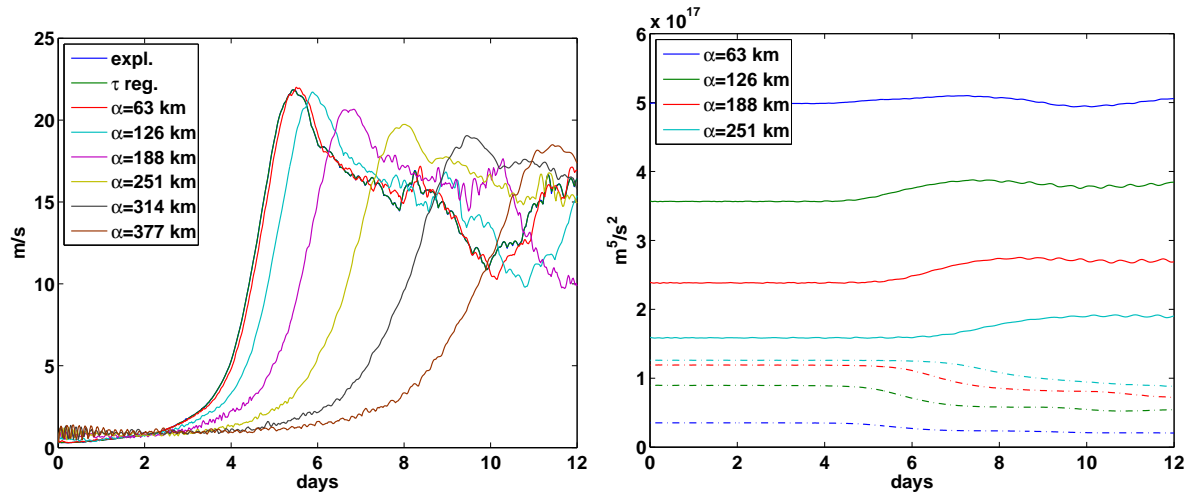

FIGURE 4.10. *Effect of the regularization parameter on the onset of the instability for the shear flow test case. Left: maximum meridional velocity for SW-0 (blue, practically coinciding with SW-τ), SW-τ with $\beta = 94.17\,km$ (green) and SW-α for varying α (see figure the legend). Right: time evolution of the two components of the kinetic energy of the SW-α system for four different choices of α, gradient kinetic energy, dash-dot line, and velocity kinetic energy, solid line.*

velocity regularized system for the four cases of α equal to $63\,km$, $126\,km$, $188\,km$, and $251\,km$. It can be noted that $E_{\alpha,\mathbf{u}}$ decreases for increasing values of α, while $E_{\alpha,\nabla}$ increases for increasing values of α. Moreover, as already mentioned, regardless of the value of α, the onset of the instability is associated with a decrease of $E_{\alpha,\nabla}$ which is almost compensated by an increase of the velocity energy term; the energy balance being closed by a small increase of the potential energy, not shown in the plot.

4.3. Rossby–Haurwitz Wave. We consider here the classical test case 6 from [40], where the propagation of a Rossby–Haurwitz wave is considered. The results of the integration of the regularized problem at time $11.76\,days$, on an icosahedral grid with average resolution of approximately $500\,km$, are plotted in Fig. 4.11, together with a reference explicit integration and the analytic solution of the barotropic vorticity equation, for comparison. The time step is $2400\,s$ for both SW-α and SW-τ and $900\,s$ for SW-0. For the regularized computations, the smoothing lengths are $\alpha = 400\,km$ and $\beta = 386\,km$. An off centering is used for the space regularized system with $\tau_\varepsilon = 4\,hours$, while no off-centering is used for the time regularized run. To simplify comparisons with results in the literature, the free surface elevation in SW-α is initialized with the same profile used for SW-0 and SW-τ. Concerning SW-τ, the computed solution is almost indistinguishable from the reference explicit run, which in turn shows an overall similarity with the analytic solution. In fact, the differences between the SW-0 solution and the analytic one are due partly to the fact that this latter considers a simplified, nondivergent barotropic case, partly to the instability of the wave in the compressible case and partly to the rather coarse resolution, and are within the range of deviations usually observed for this test, as

shown for instance in [39]. Concerning SW-α, two points should be mentioned. The first one is the fact that the space regularization results in a significant change of the phase velocity of the wave, the net effect of which is a higher eastward propagation. This corresponds to a slower westward propagation of the wave with respect to the background flow, in agreement with what discussed in [41] concerning the slowing down of Rossby waves. The second point is that SW-α determines a delay in the break-down of the wave pattern, a fact that is confirmed by the analysis of the complete time evolution of the flow. Such an effect is consistent with the results reported in § 4.2.1. Notice also the appearance of the local maxima at $\pm 50°$, common to SW-0, SW-α and SW-τ. The energy balance for this test case is also reported in Fig. 4.12 for a much longer time interval of $100\,days$. In the time regularized system the total energy is well preserved, with small deviations which are analogous to those of a control explicit integration (not reported here). For the space regularized system, the total energy initially increases during the first $20\,days$, and remains constant during the rest of the time span. The gradient kinetic energy decreases during the first part of the simulation, and then remains constant, a pattern which is common to all our numerical results. For this test case, the combined velocity and pressure regularization (2.14) has also
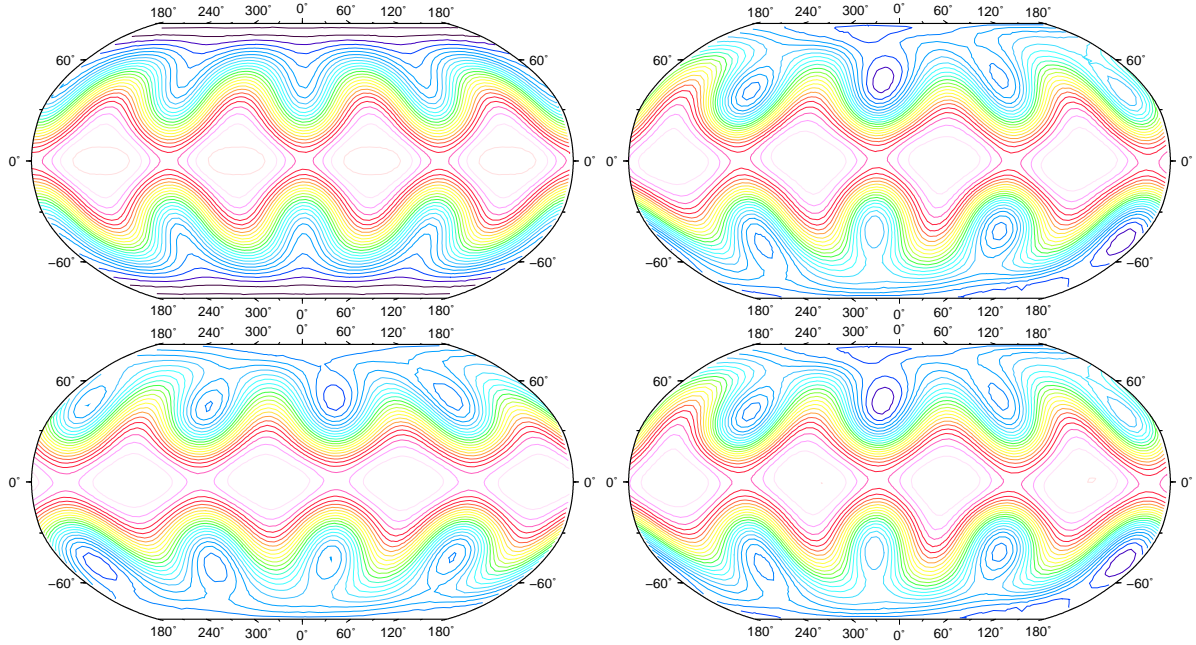

FIGURE 4.11. *Rossby–Haurwitz wave test case as in [40], free surface height after* 11.76 *days simulation time, contour lines from* 8030 *m to* 10530 *m with contour intervals of* 100 *m. Analytic solution of the barotropic vorticity equation (top, left), reference explicit solution with* $\Delta t = 900\,s$ *(top right), space and time regularized solutions (bottom left and right, respectively), both with* $\Delta t = 2400\,s$.

been tested using a time step of $2400\,s$, smoothing lengths $\alpha = \beta = 400\,km$ and no off-centering. The results (not shown here) are very similar to the SW-τ case, thus confirming that the propagation of the Rossby-Haurwitz wave is not modified in this system.

4.4. Decaying turbulence simulation. In this section, we analyze the evolution of the energy and enstrophy spectra in a planar decaying turbulence experiment. Compared to previous works on SW-α, the results presented here are the first ones including the compressibility effect associated with the presence of a free surface. Except for the fact that we use second order Laplacian diffusion, rather than hyper-diffusion, the experiment setup is similar to [9], and it is as follows. The initial depth $h(x, y, 0)$ has mean $H_0 = 4000\,m$, yielding the Rossby deformation radius $L_D = 3220\,km$, and a random distribution peaked at total wavenumber $K_I = 0.0054\,km^{-1}$, with corresponding wave length $\lambda_I = \frac{1}{4}\frac{L_x+L_y}{2}$, and standard deviation $13.49\,m$. The velocity field is initialized, as in the other experiments, by enforcing linear geostrophic balance, yielding for $|\mathbf{u}|$ a mean value $U = 22.33\,ms^{-1}$ and a standard deviation $13.49\,ms^{-1}$. The final time of the integration is $T^{fin} = 100\,days$. The mean value $\langle|\mathbf{u}|\rangle$, where $\langle\cdot\rangle$ indicates spatial averaging at a fixed time level, changes only by 17% during the whole integration, so
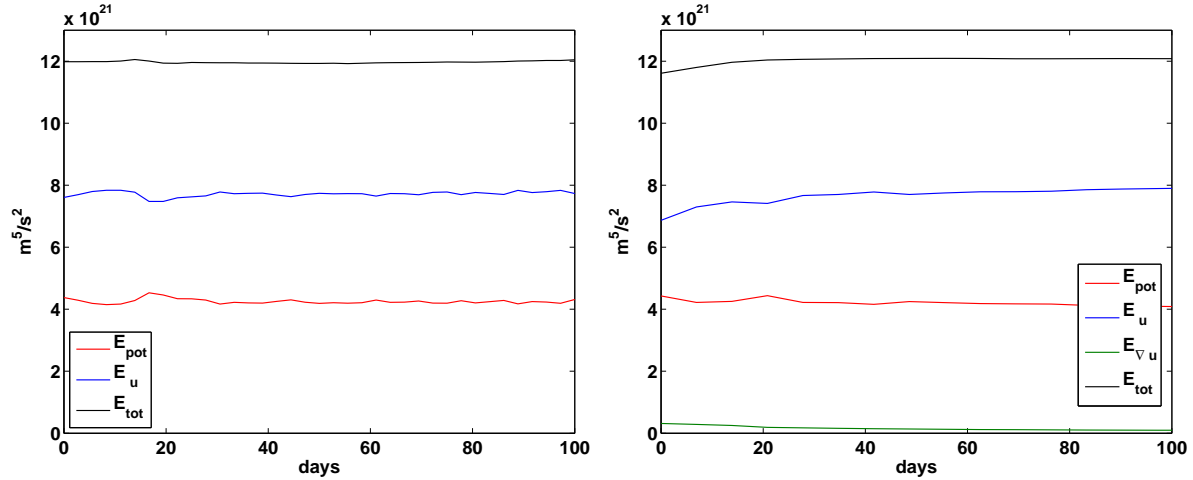
FIGURE 4.12. *Rossby–Haurwitz wave test case as in [40], energy balance for a 100 days run. Potential energy (red), kinetic energy* **u** *(blue), kinetic energy* grad **u** *(green) and total energy (black) for the time regularized system (left) and the space regularized system (right).*

that U is a significant velocity scale throughout the experiment and the Froude number is

$$F = \frac{U}{\sqrt{gH_0}} = 0.113.$$

Concerning the Rossby number, we redefine it as

$$R = \frac{\langle |\zeta| \rangle}{f},$$

as in [9]. At the initial time level we have $R = 10.72$, this number however rapidly decreases and we have $R = 0.5$ at time $10\,days$, $R = 0.321$ at time $30\,days$ and $R = 0.267$ at times larger than $50\,days$. In general, our setup fits into the "mostly rotational, moderate rotation" (RM) regime described in [9]. Concerning the values of the viscosity and the regularization parameters, four configurations are considered: SW-0 with $\nu = 446\,m^2s^{-1}$, SW-0 with $\nu = 891\,m^2s^{-1}$, SW-α with $\nu = 446\,m^2s^{-1}$ and $\alpha = 20\,km$ and SW-τ with $\nu = 446\,m^2s^{-1}$ and $\beta = 17.83\,km$. The spatial resolution is $\lambda = 19.53\,km$, and the time step is $60\,s$ for both SW-0 experiments, $120\,s$ for SW-α and $180\,s$ for SW-τ. No off-centering is introduced.

4.4.1. Definition of the energy and enstrophy spectra. Energy and enstrophy are computed generalizing the expressions provided in [9] to SW-α and SW-τ, so that the compressibility of the flow is fully taken into account. To this end, we start by considering the linearized SW-α system, rewritten for convenience in terms of relative vorticity $\zeta = \mathbf{k} \cdot \nabla \times \mathbf{u}$, divergence $\delta = \nabla \cdot \mathbf{u}$ and geopotential $\phi = g\tilde{h}$,

$$
\begin{aligned}
\partial_t \zeta + f \left(1 - \alpha^2 \Delta\right)^{-1} \delta &= 0 \\
\partial_t \delta - f \left(1 - \alpha^2 \Delta\right)^{-1} \zeta + \Delta\phi &= 0 \\
\partial_t \phi + gH_0 \left(1 - \alpha^2 \Delta\right)^{-1} \delta &= 0.
\end{aligned}
\tag{4.3}
$$

This system has a complete set of eigenmodes which can be grouped in two classes: the potentio-vortical modes, denoted by V, and the inertio-gravitational modes, denoted by G. Using the notation $\boldsymbol{\varphi} = [\zeta, \delta, \phi]^T$ and the coefficients D and F introduced in (3.15), the potentio-vortical modes are of the form

$$\omega_0 = 0, \qquad \boldsymbol{\varphi}_K^0(x, y, t) = \begin{bmatrix} f \\ 0 \\ -gH_0 \frac{F}{D} \end{bmatrix} e^{i(kx+ly-\omega_0 t)},$$

where $K^2 = k^2 + l^2$, and they are stationary ($\omega = 0$), nondivergent ($\delta = 0$) and geostrophic ($\Delta\phi = f\left(1 - \alpha^2\Delta\right)^{-1}\zeta$). The inertio-gravitational modes are of the form

$$\omega_{1,2} = \pm\sqrt{D + F}, \qquad \boldsymbol{\varphi}_K^{1,2}(x,y,t) = \begin{bmatrix} \mp i\dfrac{f}{\sqrt{\frac{D}{F}+1}} \\ f \\ \mp i\dfrac{gH_0}{\sqrt{\frac{D}{F}+1}} \end{bmatrix} e^{i(kx+ly-\omega_{1,2}t)}$$

and are divergent and ageostrophic. We then observe that (4.3) has the two quadratic invariants

$$E'_\alpha(\boldsymbol{\varphi}) = \frac{1}{2}\int_\Omega \left(\frac{\phi^2}{g} + H_0\left(|\tilde{\mathbf{u}}|^2 + \alpha^2|\nabla\tilde{\mathbf{u}}|^2\right)\right) d\Omega \tag{4.4}$$

and

$$S'(\boldsymbol{\varphi}) = \frac{1}{2}\int_\Omega q'^2 d\Omega, \tag{4.5}$$

with $q' = \zeta - \frac{f}{gH_0}\phi$, which are approximations of the invariants of the full SW-α system for deviations of $\tilde{h}$ small compared to the mean value H_0. Being quadratic, E'_α and S' can be expressed, for a generic configuration $\boldsymbol{\varphi}$, as the sum of the contributions of the eigenmodes $\boldsymbol{\varphi}_K^i$, for $i = 0, 1, 2$. More precisely, after expanding $\boldsymbol{\varphi}$ into the eigemodes $\boldsymbol{\varphi}_K^i$, both potentio-vortical modes and inertio-gravity modes contribute to E'_α, while only the formers contribute to S', since q' vanishes for $\boldsymbol{\varphi}_K^{1;2}$. This allows us to define a potentio-vortical energy spectrum as the collection of the contributions to E'_α from $\boldsymbol{\varphi}_K^0$, an inertio-gravitational energy spectrum as the collection of the contributions to E'_α from $\boldsymbol{\varphi}_K^{1;2}$ and an enstrophy spectrum as the collection of the contributions to S' from $\boldsymbol{\varphi}_K^0$. After some algebra we obtain the one-dimensional spectra

$$E'_{\alpha_V}(\bar{K}) = \frac{1}{\delta K}\sum_{\bar{K}-\frac{\delta K}{2} < K \leq \bar{K}+\frac{\delta K}{2}} \frac{1}{2}gH_0^2\frac{1}{\frac{D}{F}+1}\left|-\frac{\zeta_K}{f} + \frac{\phi_K}{gH_0}\right|^2 \tag{4.6}$$

$$E'_{\alpha_G}(\bar{K}) = \frac{1}{\delta K}\sum_{\bar{K}-\frac{\delta K}{2} < K \leq \bar{K}+\frac{\delta K}{2}} \frac{1}{2}gH_0^2\frac{F}{D}\left(\left|\frac{\delta_K}{f}\right|^2 + \frac{1}{\frac{D}{F}+1}\left|-\frac{\zeta_K}{f} - \frac{D}{F}\frac{\phi_K}{gH_0}\right|^2\right) \tag{4.7}$$

and

$$S'_V(\bar{K}) = \frac{1}{\delta K}\sum_{\bar{K}-\frac{\delta K}{2} < K \leq \bar{K}+\frac{\delta K}{2}} \frac{1}{2}f^2\left|-\frac{\zeta_K}{f} + \frac{\phi_K}{gH_0}\right|^2, \tag{4.8}$$

where ζ_K, δ_K and ϕ_K are the spectral components of ζ, δ and ϕ, respectively. Formulas (4.6–4.8) generalize (10–13) of [9] to the case of SW-α.

A similar procedure can be followed for SW-τ. In this case, we first consider the linearized system

$$\begin{aligned} \partial_t\zeta + f\delta &= 0 \\ \partial_t\delta - f\zeta + \Delta\left[\left(1 - \beta^2\Delta\right)^{-1}\left(\phi - \mathcal{B}\beta^2 f\zeta\right)\right] &= 0 \\ \partial_t\phi + gH_0\delta &= 0, \end{aligned} \tag{4.9}$$

where $\mathcal{B}$ is defined as in § 3.3.2. As for (4.3), system (4.9) has a complete set of eigemodes which can be grouped in two classes: the potentio-vortical modes, and the inertio-gravitational modes. Using the coefficients P and Q introduced in (3.20), the potentio-vortical modes are of the form

$$\omega_0 = 0, \qquad \boldsymbol{\varphi}_K^0(x,y,t) = \begin{bmatrix} f \\ 0 \\ -gH_0\frac{Q}{P} \end{bmatrix} e^{i(kx+ly-\omega_0 t)},$$

and are stationary, nondivergent, geostrophic and coincide with the potentio-vortical modes of SW-0 for $\mathcal{B} = 1$. The inertio-gravitational modes are of the form

$$\omega_{1,2} = \pm\sqrt{P+Q}, \qquad \varphi_K^{1,2}(x,y,t) = \begin{bmatrix} \mp i\sqrt{\frac{1+\beta^2 K^2}{1+(1-\mathcal{B})\beta^2 K^2}}\frac{f}{\sqrt{\frac{P}{Q}+1}} \\ f \\ \mp i\sqrt{\frac{1+\beta^2 K^2}{1+(1-\mathcal{B})\beta^2 K^2}}\frac{gH_0}{\sqrt{\frac{P}{Q}+1}} \end{bmatrix} e^{i(kx+ly-\omega_{1,2}t)}$$

and are divergent and ageostrophic. We then observe that (4.9) has the two quadratic invariants (4.5) and

$$E_\tau'(\varphi) = \frac{1}{2}\int_\Omega \left(H_0|\mathbf{u}|^2 + \frac{\xi}{g}\left(\tilde{\phi}^2 + \beta^2|\nabla\tilde{\phi}|^2\right)\right) d\Omega, \tag{4.10}$$

with

$$\xi = \left(1 - \mathcal{B}\frac{\beta^2 f^2}{gH_0}\right)^{-1}.$$

Proceeding as for SW-α, we obtain the one-dimensional energy spectra

$$E_{\tau_V}'(\bar{K}) = \frac{1}{\delta K}\sum_{\bar{K}-\frac{\delta K}{2}<K\leq\bar{K}+\frac{\delta K}{2}} \frac{1}{2}gH_0^2 \frac{\xi}{1+(1-\mathcal{B})\beta^2 K^2}\frac{1}{\frac{P}{Q}+1}\left|-\frac{\zeta_K}{f}+\frac{\phi_K}{gH_0}\right|^2 \tag{4.11}$$

$$\begin{aligned} E_{\tau_G}'(\bar{K}) &= \frac{1}{\delta K}\sum_{\bar{K}-\frac{\delta K}{2}<K\leq\bar{K}+\frac{\delta K}{2}} \frac{1}{2}gH_0^2\frac{Q}{P}\left(\frac{1}{1+(1-\mathcal{B})\beta^2 K^2}\left|\frac{\delta_K}{f}\right|^2\right. \\ &\left. +\frac{1}{1+\beta^2 K^2}\frac{1}{\frac{P}{Q}+1}\left|-\frac{\zeta_K}{f}-\frac{P}{Q}\frac{\phi_K}{gH_0}\right|^2\right), \end{aligned} \tag{4.12}$$

while the enstrophy spectrum is given by (4.8). The energy and enstrophy spectra of the initial condition for the various configurations are plotted in Fig. 4.13.
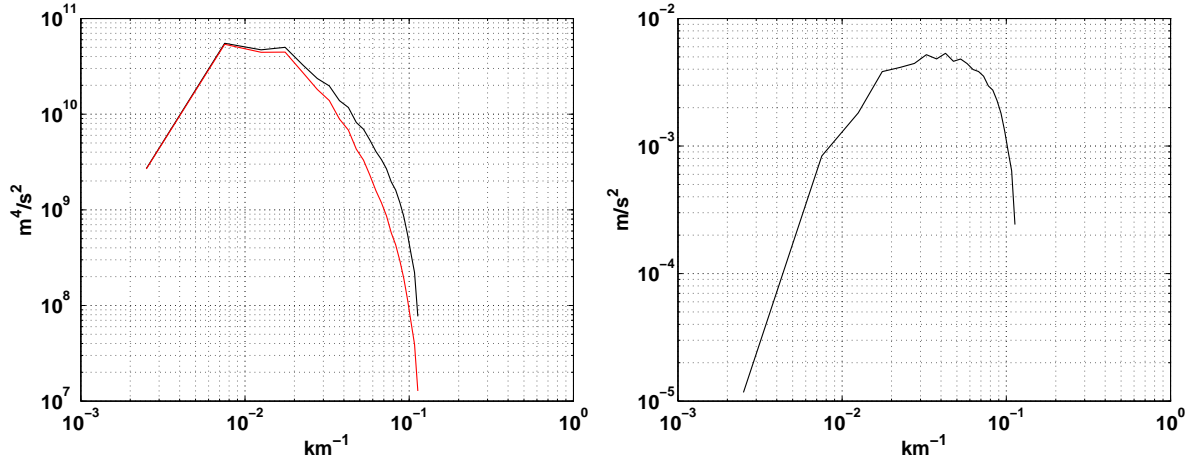

FIGURE 4.13. *Decaying turbulence test case, energy and enstrophy spectra of the initial configuration. Left: E_V' for SW-0, black, and SW-α, red; for SW-τ, E_{τ_V}' coincides with SW-0. Right: S' for SW-0, which essentially coincides with the cases SW-α and SW-τ.*

4.4.2. Discussion of the results. We first consider the time evolution of the total energy E' and enstropy S', represented in Fig. 4.14 left and right, respectively. The main conclusion that can be drawn from these plots is that the dissipation rates of E' and S' only depend on the viscosity coefficient, with the three experiments at $\nu = 446m^2s^{-1}$ having the same decay rate, with the exception of E'_α which is dissipated at a lower rate during the first 10 days of integration. Hence, neither of the examined regularizations enhances the overall dissipation. We also observe that only 30% of the initial energy is dissipated after 100 days, while only 0.2% of the initial potential enstrophy is left at the same time.
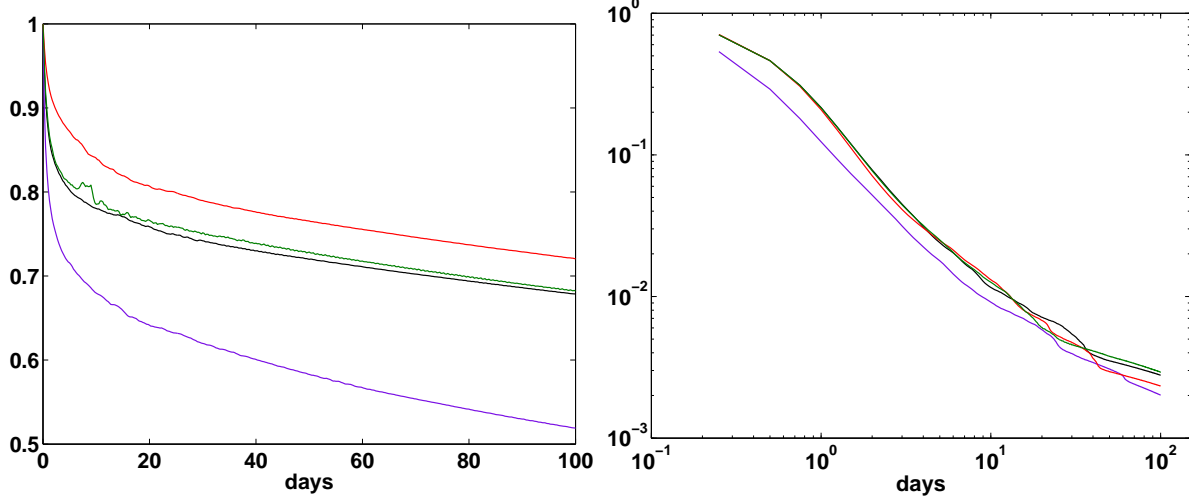
FIGURE 4.14. *Time evolution of the total energy E' (left, linear scale), and potential enstrophy S' (right, logarithmic scale) for the decaying turbulence experiment, with values normalized by the initial conditions $E'(t = 0)$ and $S'(t = 0)$. Results for SW-0, $\nu = 446m^2s^{-1}$, black, SW-0, $\nu = 891m^2s^{-1}$, purple, SW-α, red, and SW-τ, green.*

Concerning the qualitative evolution of the flow, we notice that all the simulations finally reach a two vortex configuration, after which no significant changes appear. Such a configuration is reached at time level $46\,days$ for SW-0, $\nu = 446\,m^2s^{-1}$, $60\,days$ for SW-0, $\nu = 891\,m^2s^{-1}$, $44\,days$ for SW-α and $47\,days$ for SW-τ.

The spectral distributions of E'_V, E'_G and S' at time levels $2\,days$, $5\,days$, $10\,days$, $25\,days$, $50\,days$ and $100\,days$ are plotted in figures 4.15, 4.16 and 4.17. More precisely, snapshots of the flow are used at time levels $2\,days$ and $5\,days$, while for the larger time levels a low pass filter with cutoff frequency of two days has been applied separately to the time evolution of each wavenumber before evaluating the spectral distribution. This is done in order to remove the short term differences which arise in the spectra as the number of vortices decreases due to the inverse cascade, and is a surrogate of performing ensemble simulation, which would go beyond our current computational possibilities. Figure 4.15 shows that, on the one hand, E'_{α_V} is close the SW-0 spectrum with the same viscosity at low wave numbers, while it is lower at high wave numbers. With our setup, in particular, the effect of the space regularization at high wave numbers is comparable to the effect of doubling the viscosity coefficient in SW-0. This result is similar to that reported in [5], concerning the sharper roll-off of the energy spectrum of the regularized Navier–Stokes equations. On the other hand, E'_τ is very close to the SW-0 spectrum with the same viscosity at all wave numbers, so that we can conclude that the time regularization has no effect on the potentio-vortical modes. The situation is different when looking at the inertio-gravitational modes, as shown in Fig. 4.16. Here, it can be seen that E'_{α_G} and E'_{τ_G} both deviate from the spectrum of SW-0 at the same viscosity approximately at wave number $0.02\,km^{-1}$, and show a further change in the slope at wave number $0.07\,km^{-1}$. This effect is different from the effect of increasing the viscosity coefficient. Somewhat surprisingly, E'_{α_G} always contains more energy at high wave numbers compared to SW-0 and SW-τ, as opposite to the effect of the space regularization on the incompressible modes. This fact, if confirmed by further tests, might be related, on the one hand, to the fact that, for a fixed smoothing length, a larger time step can be taken for SW-τ than for SW-α (see the previous sections § 4.1, § 4.2 and § 4.3), and might indicate, on the other hand, a difficulty in using the Lagrangian averaging idea when

dealing with compressible flows. Our results, however, also suggest that a coupling of the velocity and pressure regularizations, where the former is applied only to the incompressible component of the flow and the latter is applied only to its divergent component, might overcome such a difficulty, since SW-τ results in a tail of the spectrum which is analogous to the SW-0 case. We also mention that in our results $E_V' \gg E_G'$ at all but the highest wave numbers, so that the spectrum of the total energy is dominated by the potentio-vortical component. Finally, concerning the potential enstrophy spectra, figure 4.17 shows that the behavior of SW-α and SW-τ is very similar to the case SW-0 with equal viscosity, thus confirming the picture emerging from Fig. 4.14, up to time level $50\,days$. For larger times, SW-α and SW-τ seem to deviate from the SW-0, $\nu = 446\,m^2 s^{-1}$ case at wave numbers higher than $0.2\,km^{-1}$, and remain close to each other. However, a precise understanding of this effect requires further investigation.

5. Summary of Main Results. In this article, we have considered two modified (regularized) versions of the shallow water equations, showing how they can be discretized in a natural way within the finite difference formulation adopted for the ICON GCM and analyzing their effect on the computed solution in a series of idealized test cases. The first modified system is the Lagrangian averaged α shallow water system, which involves the use of a regularized advection velocity and which has been recently proposed as a turbulence parametrization for ocean models in order to avoid an excessive damping of the computed solution. The second modified system is the pressure regularized τ shallow water system, which provides an alternative to traditional semi-implicit time integration schemes and which results in larger freedom in the design of the time integrator and in a better treatment of nearly geostrophic flows. The main outcomes of our investigation are as follows. First, both regularizations efficiently slowdown the high frequency gravity waves and, therefore, allow much larger time steps in the time integration compared to a standard explicit approach. The stable time step for the pressure regularized system then turns out to be larger that that of the velocity regularized one. In most cases, stability can be retained without introducing any off-centering; for those cases where such a damping mechanism is required, a way to incorporate the off-centering in the regularization approach has been proposed. The computational results for SW-τ are very similar to those obtained for SW-0, with discrepancies due to the different propagation of the short gravity waves. The results obtained for SW-α, although showing an overall similarity with the reference SW-0 case, present two types of differences: a behavior similar to the SW-τ case characterizes the divergent, gravity wave component of the flow, and further deviations can be observed in the vortical component. These latter deviations involve: different position of the vortical structures having a scale comparable to α, different development of flow instabilities, different propagation of Rossby-Haurwitz waves and different energy spectra, with a sharper roll-off at high wave numbers. We plan to investigate the consequences of such effects on more realistic flow configurations, involving also baroclinicity, in future research work. Finally, for all the test cases, numerical evidence has been provided that the proposed numerical discretization correctly reproduces the nondissipative nature of the two continuous regularized systems.

REFERENCES

[1] D. Andrews and M. McIntyre, *Exact theory of non-linear waves on a lagrangian-mean flow*, Journal Of Fluid Mechanics, 89 (1978), pp. 609–646.

[2] L. Berselli, T. Iliescu, and W. Layton, *Mathematics of large eddy simulation of turbulent flows*, Springer, Berlin, 2005.

[3] L. Bonaventura, L. Kornblueh, T. Heinze, and P. Ripodas, *A semi-implicit method conserving mass and potential vorticity for the shallow water equations on the sphere*, Int. J. Numer. Methods Fl., 47 (2005), pp. 863–869.

[4] L. Bonaventura and T. Ringler, *Analysis of discrete shallow-water models on geodesic Delaunay grids with C-type staggering.*, Mon. Wea. Rev., 133 (2005), pp. 2351–2373.

[5] S. Chen, D. Holm, L. Margolin, and R. Zhang, *Direct numerical simulations of the Navier–Stokes alpha model*, Physica D: Nonlinear Phenomena, 133 (1999), pp. 66–83.
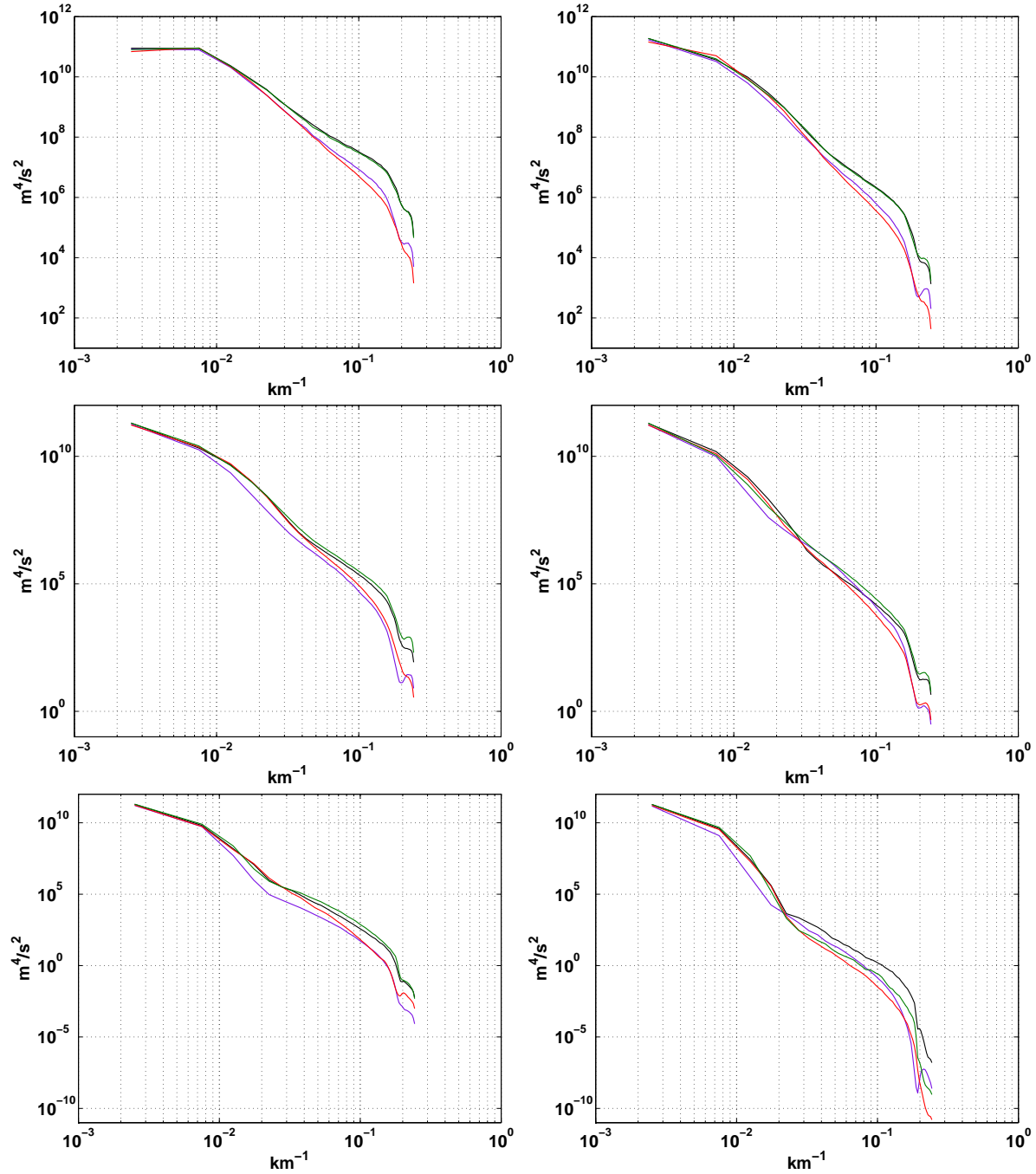
FIGURE 4.15. *Spectra of the potentio-vortical energy E'_V for SW-0, $\nu = 446 m^2 s^{-1}$, black, SW-0, $\nu = 891 m^2 s^{-1}$, purple, SW-α, red, and SW-τ, green. Results at time levels 2 days and 5 days (first row, left and right, respectively), 10 days and 25 days (second row) and 50 days and 100 days (third row).*

[6] X. CHEN AND E. FRIED, *Influence of the dispersive and dissipative scales α and β on the energy spectrum of the Navier–Stokes $\alpha\beta$ equations*, Phys. Rev. E, 78 (2008), pp. 046317–10.

[7] M. CULLEN, *Large scale atmosphere/ocean flow*, Imperial College Press, 2006.

[8] R. DI LISIO, E. GRENIER, AND M. PULVIRENTI, *On the regularization of the pressure field in compressible Euler equations.*, Ann. Sc. Norm. Super. Pisa, Cl. Sci., IV. Ser., 24 (1997), pp. 227–238.

[9] M. FARGE AND R. SADOURNY, *Wave vortex dynamics in rotating shallow-water*, J. Fluid Mech., 206 (1989), pp. 433–462.

[10] C. FOIAS, D. HOLM, AND E. TITI, *The Navier–Stokes-alpha model of fluid turbulence*, Physica D: Nonlinear Phe-
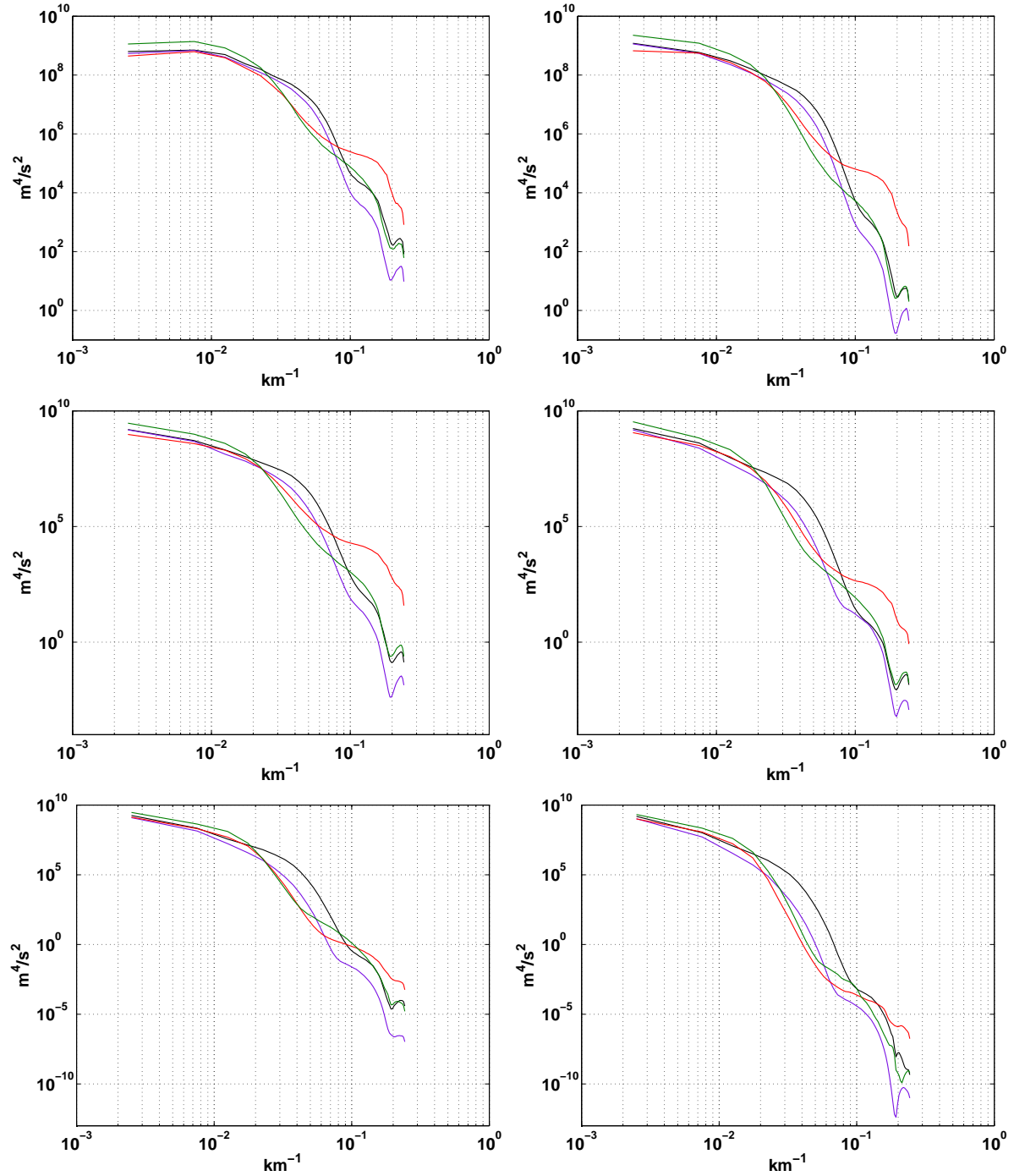
FIGURE 4.16. *Spectra of the inertio-gravitational energy E'_G for SW-0, $\nu = 446 m^2 s^{-1}$, black, SW-0, $\nu = 891 m^2 s^{-1}$, purple, SW-α, red, and SW-τ, green. Results at time levels 2 days and 5 days (first row, left and right, respectively), 10 days and 25 days (second row) and 50 days and 100 days (third row).*

nomena, 152-153 (2001), pp. 505–519.

[11] E. FRIED AND M. E. GURTIN, *Turbulent kinetic energy and a possible hierarchy of length scales in a generalization of the Navier–Stokes alpha theory*, Phys. Rev. E, 75 (2007), p. 056306.

[12] B. GEURTS AND D. HOLM, *Regularization modeling for large-eddy simulation*, Phys. Fluids, 15 (2003), pp. L13–L16.

[13] ——, *Leray and LANS-α modelling of turbulent mixing*, J. Turb., 7 (2006), pp. N10–.

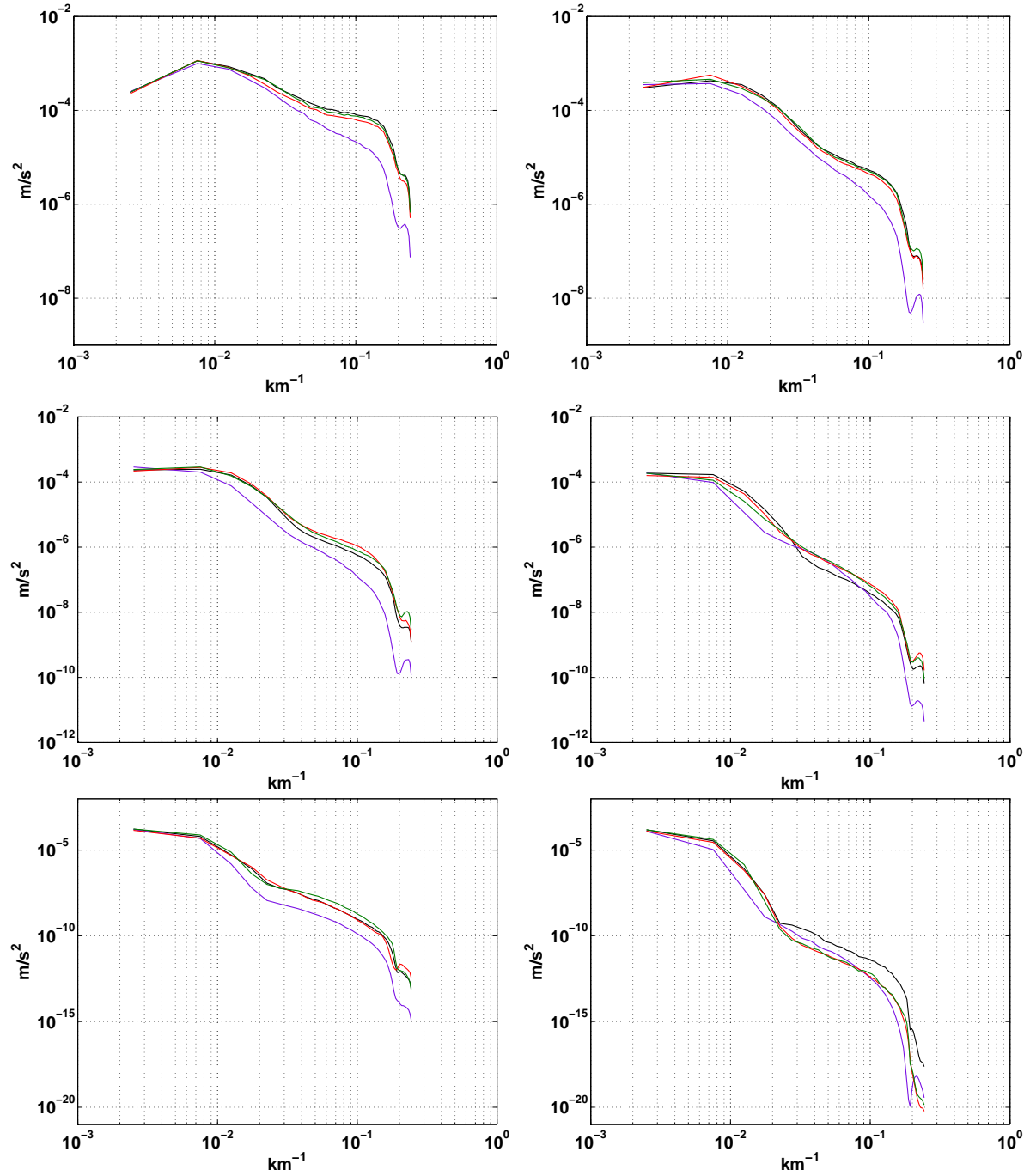[14] B. GEURTS, A. KUCZAJ, AND E. TITI, *Regularization modeling for large-eddy simulation of homogeneous isotropic*

FIGURE 4.17. *Spectra of the potential enstrophy S' for SW-0, $\nu = 446m^2 s^{-1}$, black, SW-0, $\nu = 891m^2 s^{-1}$, purple, SW-α, red, and SW-τ, green. Results at time levels $2\,days$ and $5\,days$ (first row, left and right, respectively), $10\,days$ and $25\,days$ (second row) and $50\,days$ and $100\,days$ (third row).*

decaying turbulence, J. Phys. A: Mathematical and Theoretical, (2008), p. 344008.

[15] F. GIRALDO AND M. RESTELLI, *A study of spectral element and discontinuous Galerkin methods for the Navier–Stokes equations in nonhydrostatic mesoscale atmospheric modeling: Equation sets and test cases*, J. Comput. Phys., 227 (2008), pp. 3849–3877.

[16] J. GUERMOND, J. ODEN, AND S. PRUDHOMME, *An interpretation of the Navier–Stokes-alpha model as a frame-indifferent Leray regularization*, Physica D: Nonlinear Phenomena, 177 (2003), pp. 23–30.

[17] M. E. GURTIN, *An introduction to continuum mechanics*, Academic Press, 1982.

[18] M. Hecht, D. Holm, M. Petersen, and B. Wingate, *Implementation of the LANS-α turbulence model in a primitive equation ocean model*, J. Comput. Phys., 227 (2008), pp. 5691–5716.

[19] D. Holm, *Fluctuation effects on 3D Lagrangian mean and Eulerian mean fluid motion*, Physica D: Nonlinear Phenomena, 133 (1999), pp. 215–269.

[20] D. Holm, J. Marsden, and T. Ratiu, *The Euler–Poincaré equations in geophysical fluid dynamics*, tech. rep., Isaac Newton Institute for Mathematical Sciences, 1998.

[21] D. Holm and B. Wingate, *Baroclinic instabilities of the two-layer quasigeostrophic alpha model.*, J. Phys. Ocean., 35 (2005), pp. 1287–1296.

[22] D. D. Holm, C. Jeffery, S. Kurien, D. Livescu, M. A. Taylor, and B. A. Wingate, *The LANS–α model for computing turbulence*, Los Alamos Science 29, Los Alamos National Laboratory, 2005.

[23] T. Hundertmark and S. Reich, *A regularization approach for a vertical-slice model and semi-Lagrangian Störmer–Verlet time stepping*, Q. J. R. Meteorol. Soc., 133 (2007), pp. 1575–1587.

[24] J. Leray, *Sur le mouvement d'un liquide visqueux emplissant l'espace*, Acta Mathematica, 63 (1934), pp. 193–248.

[25] E. Lunasin, S. Kurien, M. Taylor, and E. Titi, *A study of the navier–stokes-α model for two-dimensional turbulence*, J. Turb., 8 (2007), pp. N30–.

[26] D. Majewski, D. Liermann, P. Prohl, B. Ritter, M. Buchhold, T. Hanisch, G. Paul, W. Wergen, and J. Baumgardner, *The operational global icosahedral–hexagonal gridpoint model GME: Description and high-resolution tests.*, Mon. Wea. Rev., 130 (2002), pp. 319–.

[27] K. Mohseni, B. Kosović, S. Shkoller, and J. Marsden, *Numerical simulations of the Lagrangian averaged Navier–Stokes equations for homogeneous isotropic turbulence*, Phys. Fluids, 15 (2003), pp. 524–544.

[28] D. Montgomery and A. Pouquet, *An alternative interpretation for the holm "alpha model"*, Phys. Fluids, 14 (2002), pp. 3365–3366.

[29] B. Nadiga and S. Shkoller, *Enhancement of the inverse-cascade of energy in the two-dimensional Lagrangian-averaged Navier–Stokes equations*, Phys. Fluids, 13 (2001), pp. 1528–1531.

[30] J. Pedlosky, *Geophysical fluid dynamics*, Springer, Berlin, 1987.

[31] M. Petersen, M. Hecht, and B. Wingate, *Efficient form of the LANS-α turbulence model in a primitive-equation ocean model*, J. Comput. Phys., 227 (2008), pp. 5717–5735.

[32] M. Rančić, R. Purser, and F. Mesinger, *A global shallow-water model using an expanded spherical cube: Gnomonic versus conformal coordinates*, Q. J. R. Meteorol. Soc., 122 (1996), pp. 959–982.

[33] S. Reich, *Linearly implicit time stepping methods for numerical weather prediction*, BIT Numerical Mathematics, 46 (2006), pp. 607–616.

[34] S. Reich, N. Wood, and A. Staniforth, *Semi-implicit methods, nonlinear balance, and regularized equations*, Atmos. Sci. Lett., 8 (2007), pp. 1–6.

[35] E. Roeckner, G. Bäuml, L. Bonaventura, R. Brokopf, M. Esch, M. Giorgetta, S. Hagemann, I. Kirchner, L. Kornblueh, E. Manzini, A. Rhodin, U. Schlese, U. Schulzweida, and A. Tompkins, *The atmospheric general circulation model ECHAM5. Part 1: model description.*, MPI–Report 349, Max–Planck–Institute für Meteorologie, 2003.

[36] R. Spiteri and S. Ruuth, *A new class of optimal high-order strong-stability-preserving time discretization methods.*, SIAM Journal on Numerical Analysis, 40 (2002), pp. 469–.

[37] A. Staniforth and N. Wood, *Analysis of the response to orographic forcing of a time-staggered semi-Lagrangian discretization of the rotating shallow-water equations*, Q. J. R. Meteorol. Soc., 132 (2006), pp. 3117–3126.

[38] A. Staniforth, N. Wood, and S. Reich, *A time-staggered semi-Lagrangian discretization of the rotating shallow-water equations*, Q. J. R. Meteorol. Soc., 132 (2006), pp. 3107–3116.

[39] H. Wan, *Developing and testing a hydrostatic atmospheric dynamical core on triangular grids*, PhD thesis, Universität Hamburg, 2009.

[40] D. Williamson, J. Drake, J. Hack, R. Jakob, and P. Swarztrauber, *A standard test set for numerical approximations to the shallow water equations in spherical geometry*, J. Comput. Phys., 102 (1992), pp. 211–224.

[41] B. Wingate, *The maximum allowable time step for the shallow water model and its relation to time-implicit differencing.*, Mon. Wea. Rev., 132 (2004), pp. 2719–2731.